Imprint of vortical structures on the near-field pressure of a turbulent jet

Andres Adam, Dimitri Papamoschou, Christophe Bogey

Imprint of vortical structures on the near-field pressure of a turbulent jet

Andres Adam* and Dimitri Papamoschou †
University of California, Irvine, Irvine, CA, 92697, USA

Christophe Bogey‡
Laboratoire de Mécanique des Fluides et d'Acoustique, UMR CNRS 5509, F-69134, Ecully, France

The distributions of turbulent scales in a Mach 0.9 isothermal round jet are investigated for the purpose of developing linear surface-based models for the noise source that can be informed by a Reynolds-averaged Navier Stokes (RANS) solution of the flow field. The jet is calculated by large-eddy simulation (LES) which enables the computation of two-point space-time correlations throughout the jet and its near acoustic field. Time, length, and convective-velocity scales are examined on the surface of peak Reynolds stress (SPS), representing the location of the most energetic eddies, and on a "radiator surface" at the boundary between the rotational and irrotational fields. The nature of the space-time correlations is different for axial velocity fluctuations and pressure fluctuations. Velocity-based correlations appear to capture localized turbulent events, while pressure-based correlations appear dominated by the interaction of large eddies with the surrounding potential flow. The correlation length scales are larger on the radiator surface than on the SPS thus indicating that small-scale eddies do not make a significant imprint on the radiator surface. The scales associated with an emulated RANS solution of the flow are compared to the LES-based scales. Simple relationships are inferred that may aid the development of rapid predictive models.

*Ph.D. Candidate, Department of Mechanical and Aerospace Engineering, aadamalb@uci.edu, AIAA Student Member.
†Professor, Department of Mechanical and Aerospace Engineering, dpapamos@uci.edu, AIAA Fellow.
‡CNRS Research Scientist, Univ Lyon, École Centrale de Lyon, INSA Lyon, Université Claude Bernard Lyon I, CNRS, christophe.bogey@ec-lyon.fr, AIAA Associate Fellow.

Nomenclature

C	=	coefficient
D_j	=	nozzle exit diameter
g	=	magnitude of principal component of the Reynolds stress
k	=	turbulent kinetic energy
L	=	fixed-frame length scale
$\widehat{L}$	=	moving-frame length scale
M_j	=	jet exit Mach number
p	=	pressure
R	=	space-time correlation
r_i	=	radial location of inner edge of mixing layer
r_{SPS}	=	radial location of surface of peak stress
St_D	=	Strouhal number based on nozzle diameter
t	=	time
T	=	temperature
$\overline{u}_{\text{CL}}$	=	centerline mean velocity
U_c	=	convective velocity
U_j	=	jet exit velocity
u, v, w	=	velocity components in Cartesian coordinate system
x, r, ϕ	=	cylindrical coordinates, with x on jet axis
x, y, z	=	Cartesian coordinates, with x on jet axis
δ_θ	=	momentum thickness of the mixing layer
ϵ	=	turbulent dissipation
ξ, η, α	=	displacements in cylindrical coordinates
ξ, ψ, ζ	=	displacements in Cartesian coordinates
Φ	=	azimuthal scale
ρ	=	density
τ	=	time shift
$\boldsymbol{\omega}$	=	vorticity vector

I. Introduction

The turbulent exhaust of jet engines continues to be a significant contributor to aircraft noise. The research effort presented here is motivated by the need of the aerospace community for low-cost predictive models of the jet noise emission in isolated and installed configurations. For these models to have satisfactory turnaround times and become useful design tools, they need to rely on rapid solutions of the flow field such as Reynolds-Averaged Navier Stokes (RANS) simulations. The focus here is on surface-based models where the noise source is prescribed on a surface surrounding the jet flow, commonly located in the linear pressure field [1, 2]. This approach has the advantage of enabling predictions of not only propagation but also scattering from airframe surfaces using linear propagation techniques such as the boundary element method [3, 4]. In addition, surface-based models could simplify the treatment of complex multi-stream asymmetric jets that have shown promising noise reductions [5, 6].

To inform the surface-based noise source model from the RANS flow field one needs to establish physical connections between the dominant turbulent events in the vortical region of the jet and the linear pressure statistics near the edge of the jet where the surface-based model would be defined. The basic elements of this connection are depicted in Fig. 1 and represent the integration of concepts initially proposed in Refs. [6] and [7]. In a time-averaged sense, the action of the turbulent eddies that dominate sound production is represented by the statistics on the surface of peak Reynolds stress, abbreviated here as SPS. The noise source is prescribed as a distribution of random partial fields on a "radiator surface" at the edge of the jet. Each partial field is an amplitude modulated pressure wave, convected at velocity U_c, having finite axial and azimuthal extent. The convective velocity governs the radiation efficiency of the jet [6, 8, 9] and is thus deemed the most important quantity to model. Near-and far-field statistics are constructed via stochatisc superposition of the partial fields and their sound radiation. An early treatment can be seen in Ref. [10]. The simulated statistics on the radiator surface are expected to match those of the turbulent jet. Quantities of interest include the convective velocity as well as correlation length scales in the axial and azimuthal directions. Although a certain level of empiricism is expected, understanding the processes by which events in the vortical region leave a "footprint" on the radiator surface is essential for the construction of physically meaningful models.

Turbulence scales in jet shear layers have received considerable attention in the literature. One can cite the measurements obtained by hot-wire anemometry of Harper-Bourne [11] and Morris and Zaman [12], which are frequently used to inform jet noise source models. More recently, Proença *et al.* [13] performed

a comprehensive hot-wire investigation in the shear layer of various unheated single-stream jets. Studies have also been performed using particle image velocimetry (PIV), such as those by Fleury *et. al.* [14] and Pokora and McGuirk [15], which have provided detailed information on the correlations of the velocity field. However, past works have focused primarily on the jet lip line and centerline and provide little information on statistics near the edge of the jet.

Previous works by our group on LES of multi-stream jets have studied the distribution of convective velocity U_c and have made some inroads into the modeling issues outlined above [16, 17]. However, the complexity of the jet flows did not facilitate a clear understanding of the connection between vortical and near-pressure fields. In this study we have the opportunity to analyze data from a highly-resolved LES of a canonical Mach 0.9 round jet. Using two-point space-time correlations, characteristic length and velocity scales are calculated throughout the jet flow and near acoustic field. The distribution of these scales on the SPS and on the radiator surface are of particular interest. We thus aim to investigate physical connections between the core of the vortical field and the resulting pressure signature at the edge of the jet, where a linear source model would be prescribed. In addition we use the LES results to emulate the RANS flow field and evaluate the potential of using RANS to model the scales relevant to noise generation.

The present article is organized as follows. The flow conditions and numerical scheme are outlined in Section II. The definition of the turbulence scales and the methodology for their calculation are provided in Section III. The relevant surfaces analyzed in this study are defined in Section IV. The key features of the flow field are presented in Section V. The results of performing cross-correlations in the longitudinal direction, including axial length scales, are studied in Section VI. The corresponding results of cross-correlations in the azimuthal direction are studied in Section VII. Preliminary attempts at modeling the turbulence scales based on the time-averaged flow, as would be obtained with RANS, are presented in Section VIII. Concluding remarks are finally drawn in Section IX.

II. Numerical Flow Field

A. Jet Flow

We consider an isothermal, single-stream round jet at velocity $U_j = 309$ m/s, Mach number $M_j = 0.9$ and diameter-based based Reynolds number $Re_D = 10^5$. The jet originates from a pipe of constant diameter D_j and discharges into air with temperature $T_a = 293$ K and pressure $p_a = 10^5$ Pa. The pipe exit is at $x = 0$,

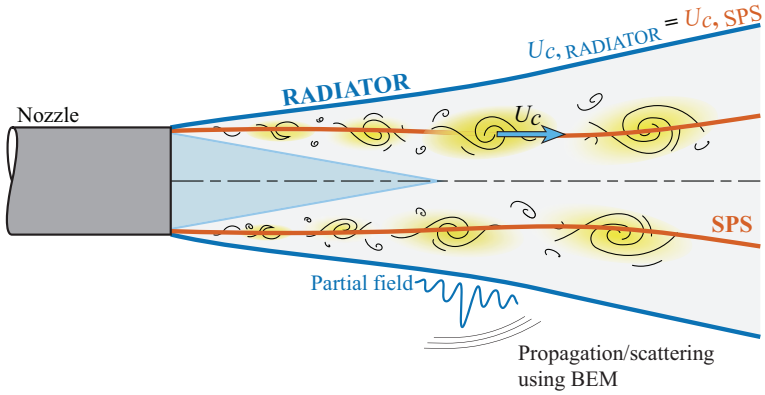

Fig. 1 Basic elements of surface-based noise source modeling.

and the pipe wall thickness is $0.053D_j$. This jet has been studied in previous works [18–22].

The pipe flow originates at $x = -D_j$, where a Blasius laminar boundary-layer profile of thickness $\delta_{BL} = 0.075D_j$ is imposed for the axial velocity. In addition, radial and azimuthal velocities are set to zero, pressure is equal to its ambient value, and the temperature is resolved by a Crocco-Busemann relation. The jet is initially disturbed by adding random low-level vortical structures uncorrelated in the azimuthal direction at $x = -0.475D_j$ inside the pipe [18]. The forcing strength is empirically set to match the nozzle-exit conditions measured in a tripped jet by Zaman [23]. The resulting mean axial velocity profile is very similar to the laminar profile imposed at the nozzle inlet, while the rms velocity profile shows peak axial turbulence intensity $u'_e/U_j = 0.0914$.

B. Numerical Methods

The numerical framework for the LES used in this work is identical to that used in previous jet simulations [18, 20–22, 24–28]. The computational code solves the three-dimensional Navier-Stokes equations in cylindrical coordinates (x, r, ϕ) using low-dissipation and low-dispersion explicit schemes. The singularity at the axis is solved by the method of Mohseni and Colonius [29]. The region near the axis also presents a restriction in time-step that is alleviated by calculating the azimuthal derivatives at coarser resolutions than those permitted by the grid [30], yielding an azimuthal resolution of $2\pi/16$. Spatial discretization is performed by fourth-order eleven-point centered finite differences, and time integration is carried out using a second-order six-stage Runge-Kutta algorithm [31]. The flow variables are filtered every time step by a sixth-order eleven-point centered explicit filter [32].

The explicit filtering used in the present simulation has the dual purpose of removing grid-to-grid oscillations and of performing as a subgrid-scale high-order dissipation model for the regions where the mesh grid is not fine enough to capture the smallest scales of turbulence. Filters and non-centered finite differences are also used near the pipe walls and grid boundaries. At the boundaries, a sponge zone combining grid stretching and Laplacian filtering is used to avoid acoustic reflections, in addition to the radiation conditions of Tam and Dong [33]. The effectiveness of this numerical framework has been assessed in previous studies in diverse cases such as subsonic jets, Taylor-Green vortices and turbulent channel flows [18, 34–37], where it has been compared against direct numerical simulations and the properties of the filtering dissipation have been examined.

C. Simulation Parameters

The simulation presented is a highly-resolved LES. Its characteristics are reported in detail in Ref. [20], where a grid-sensitivity study of the jet flow and acoustic fields is carried out, as well as in a very recent paper [22], in which the acoustic tones emerging near the nozzle are analyzed. The mesh grid contains $n_x \times n_\phi \times n_r = 2085 \times 1024 \times 512$ points, and its physical extents are $20D_j$ and $7.5D_j$ in the axial and radial dimensions respectively. The minimum mesh spacings are equal to $\Delta r = 0.0018D_j$ at $r = D_j/2$ and $\Delta x = 0.0036D_j$ at $x = 0$. The maximal mesh spacing in the jet near field is equal to $\Delta r = 0.0375$, leading to a Strouhal number of $St_D = fD_j/U_j = 5.9$ for an acoustic wave discretized by five points per wavelength, where f is the frequency.

The simulation was performed with an OpenMP-based solver using a time step $\Delta t = 0.7 \times \Delta r_{min}/c_0$ to ensure numerical stability. The simulation had an initial transient period of $87.5D_j/U_j$. The simulation time after the transient period is equal to $1250D_j/U_j$. During the stationary time, density, velocity components and pressure are recorded at a sampling frequency of $St_D = 12.8$ in eight equidistant azimuthal angles. Their Fourier coefficients in the azimuthal directions, estimated over the full section (x, r), are also saved for the first nine azimuthal modes. The statistics are averaged in the azimuthal direction, when possible. The size of the database amounts to approximately 6.5 TB. Previous work on this simulation has reported good agreement with experimental results of similar jets [21].

III. Scales in LES Flow Field

A. Space-Time Correlations

Axial length and velocity scales are computed using two-point, space-time correlations. On a meridional plane, the normalized space-time correlation of zero-mean variable f with reference the point (x,r) is

$$R_{ff}(x,r;\xi,\eta,\tau) = \frac{\overline{f(x,r,t)\, f(x+\xi,r+\eta,t+\tau)}}{\left(\overline{f^2(x,r,t)}\;\overline{f^2(x+\xi,r+\eta,t)}\right)^{1/2}} \tag{1}$$

where overline denotes time averaging. The variable f represents the fluctuating axial velocity or pressure, yielding R_{uu} or R_{pp}, respectively.

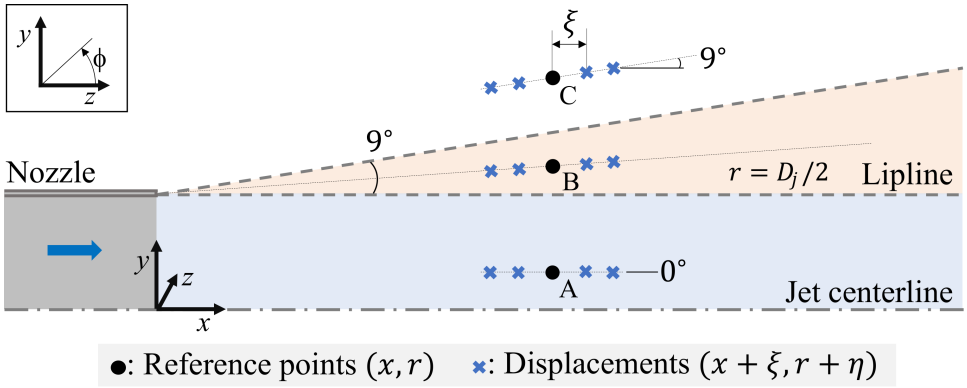

Fig. 2 Examples of stencils used in the determination of length scales. Reference points are located (A) between centerline and lipline, (B) between lipline and 9° edge, and (C) outside 9° edge.

The space-time correlations are computed using a linear stencil centered around a reference point (x,r). Even though axial correlations are sought, care must be taken that the stencil does not connect dissimilar regions of the jet. This is of particular relevance to the computation of length scales near the edge of the jet, where the transition from hydrodynamic to acoustic fields occurs within a thin layer that originates at the nozzle lip and is inclined at approximately 9° with respect to the jet centerline. A purely axial stencil near this transition layer poses the risk of extending from the acoustic to the hydrodynamic regions. Accordingly, the stencil angle, defined by $\theta = \arctan(\eta/\xi)$, follows the scheme depicted in Fig. 2. At points within the lip line $r = 0.5D_j$, the displacement is purely axial. Outside the lip line, the stencil aligns with the reference location (x,r) and the nozzle lip, up to a maximum angle of 9°. The transition layer is not known a priori and is based on the computation of the convective velocity U_c, which uses purely axial stencils. An example of space-time correlation given the reference point is plotted in Fig. 3. For a given axial separation ξ, the

correlation peaks at a time shift $\tau_{\max}$. To minimize the error due to the discrete form of the correlation, $\tau_{\max}$ is determined after fitting a seventh-order polynomial to the correlation curve for each displacement, as shown in the figure.

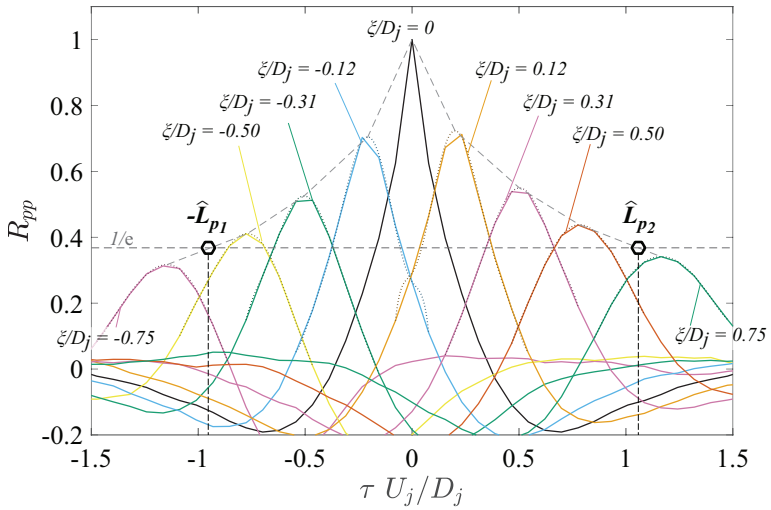

Fig. 3 Space-time correlation R_{pp} in the vortical field at $x/D_j = 2.5$ and $r/D_j = 0.5$. Dotted lines: fits by seventh-order polynomials. Dashed lines: envelope and coordinates relevant to the calculation of $\widehat{L}_p$.

B. Convective Velocity

In the space-time correlations, each discrete axial separation ξ_i around a reference location (x, r) yields a correlation that peaks at time shift $\tau_{\max,i}$. The associated phase speed is $U_{c_i} = \xi_i/\tau_{\max,i}$. The axial convective velocity at that reference location is calculated as the average of U_{c_i} extracted from the correlations whose peak values exceed 0.4. The convective velocity can be based on velocity or pressure fluctuations, yielding U_{c_u} and U_{c_p}, respectively.

C. Fixed-Frame Length Scales

The fixed-frame length scale is the axial distance L over which events remain correlated at fixed time. Following Harper-Bourne [11], Morris and Zaman [12], and Dahl [38], the length scale is the displacement ξ at which the correlation R_{ff} decays to $1/\mathrm{e}$. Noting that R_{ff} is not an even function of ξ [13], displacements ξ are taken in the negative and positive directions relative to the reference location. This procedure yields two displacements, $\xi = -L_{f_1}$ and $\xi = L_{f_2}$, that satisfy $R_{ff}(x, r; \xi, \eta(\xi), 0) = 1/\mathrm{e}$, with η and ξ linked according to

procedure outlined in Section III.A. The fixed-frame length scale is the average of of the two displacements:

$$L_f = \frac{1}{2}(L_{f_1} + L_{f_2}) \tag{2}$$

In practice, the application of Eq. (2) requires interpolation between the discrete data of the simulation. The definition of length scale used here differs from the classical definition as the integral of the correlation curve [39]. However, the two approaches yield similar results as the integral approach often terminates at the first zero crossing of R_{ff}. Comparison of the two approaches, not presented for brevity, shows that the quantitative values differ slightly but the qualitative trends are consistent.

D. Moving-Frame Length Scales

The moving-frame length scale $\widehat{L}$ is a measure of the axial distance over which turbulence remains correlated as it convects downstream. It can also be interpreted as the "length of life" of a turbulent eddy, the distance traveled until its characteristics are lost through pairing or other mechanisms. Kerhervé *et al.* [39] note that this is not a "real" length scale, but rather a product of the convective velocity and a time scale. Nevertheless, it is an intrinsic characteristic of the stochastic events of the jet and can be useful for aeroacoustic models that use a Lagrangian frame of reference. The focus now is the envelope of the correlations represented by the dashed line of Fig. 3. Similarly to the fixed-frame length scales, displacements $\xi = [-\widehat{L}_{f_1}, \widehat{L}_{f_2}]$ satisfy $R_{ff}(x, r; \xi, \eta(\xi), \tau_{\max}(\xi)) = 1/\mathrm{e}$, as illustrated in the figure. The moving-frame length scale is then defined as

$$\widehat{L}_f = \frac{1}{2}(\widehat{L}_{f_1} + \widehat{L}_{f_2}) \tag{3}$$

The values of ξ corresponding to $\widehat{L}_{f_1}$ and $\widehat{L}_{f_2}$ are linearly interpolated from the correlation maxima.

E. Azimuthal Scale

The azimuthal scale is defined for zero axial, radial, and time separations. The related two-point correlation is

$$R_{ff}(x, r, \alpha) = \frac{\overline{f(x, r, \phi, t)\, f(x, r, \phi + \alpha, t)}}{\overline{f^2(x, r, \phi, t)}} \tag{4}$$

where α is the the azimuthal separation. This formulation reflects the stationarity in azimuthal angle ϕ expected for an axisymmetric jet. For a given reference point (x, r, ϕ), the azimuthal scale Φ_f is defined by

$$R_{ff}(x, r; \alpha = \Phi_f) \; = \; 1/\mathrm{e} \tag{5}$$

The range of the azimuthal scale is $\Phi_f \in [0, \pi]$, where $\Phi_f = \pi$ indicates that R_{ff} is above the threshold of $1/\mathrm{e}$ for the entire azimuthal range. Note that in this work, the azimuthal variations of the flow field are reconstructed from the first nine Fourier modes.

IV. Relevant Surfaces

A. Surface of Peak Reynolds Stress

In the acoustic analogy model of Ref. [6] for multistream jets, it was surmised that the sound emission is strongly influenced by the dynamics of the outer shear layer. In a time-averaged sense, the action of the eddies in that shear layer is represented by the outermost peak of the Reynolds stress, resulting in the definition of the outer surface of peak Reynolds stress. The magnitude of the principal component of the Reynolds stress, normalized by the mean density, is

$$g \; = \; | < u'q' > | \tag{6}$$

where u' is the axial velocity fluctuation and q' is the transverse velocity fluctuation in the direction of the mean velocity gradient. For a single-stream round jet there is only one peak of g and the mean velocity gradient is in the radial direction. The surface is therefore named SPS (Surface of Peak Stress). It represents the locus of the most energetic eddies and can be readily detected in RANS simulations by modeling g as explained in Section VIII.

B. Radiator Surface

The radiator surface is a surface close to the edge of the jet outside of which the propagation of pressure perturbation is governed by the homogeneous linear wave equation. It is on this surface that the noise sources could be modeled in the form of linear partial fields [10]. This model would be informed by turbulence statistics of the vortical field computed by RANS. Given the impact of the convective velocity on the turbulence radiation efficiency, it is desirable that the partial fields on the radiator surface have the same

convective velocity distribution as that the underlying eddies that dominate noise emission. The specific definition for the radiator surface used in the present work is the surface near the edge of the jet where the p'-based convective velocity matches that on the SPS at the same axial location. This definition is similar to that used in previous works on multi-stream jets [16, 17] and has been shown to enclose well the vortical field of the jet.

V. Overview of the Flow Field

This section presents key features of the LES flow field that are important for scaling and interpreting the correlations that follow in sections VI and VII.

A. Mean Velocity

Isocontours of the normalized mean axial velocity, $\overline{u}/U_j$, averaged in the azimuthal direction, are plotted in Fig. 4(a). The axial distribution of the centerline mean velocity, $\overline{u}_{\mathrm{CL}}/U_j$ is plotted in Fig. 4(b) and shows good agreement with the experimental data of Lau *et al.*[40]. The end of the potential core, defined here as the point where the centerline mean axial velocity decays to $\overline{u}_{\mathrm{CL}} = 0.95U_j$, is located near $x = 7.4D_j$.

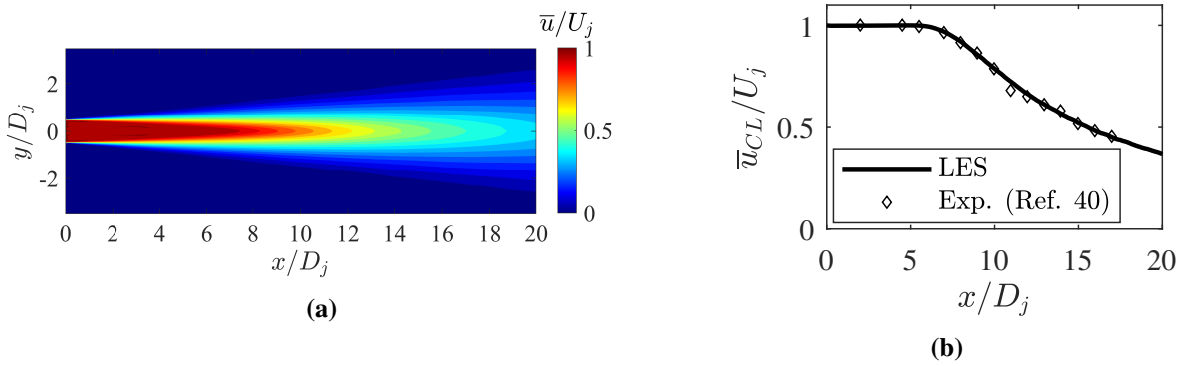

Fig. 4 Distribution of normalized mean axial velocity. (a) Isocontours on a symmetry plane; (b) axial distribution on jet centerline compared to experiments by Lau *et al.* [40].

The momentum thickness of the jet is relevant to scaling relations that follow in Sections VI and VII. To maintain the same definition within and downstream of the potential core, a generalization of the shear-layer momentum thickness is used:

$$\delta_\theta = \int_0^\infty \frac{\overline{\rho}(r)\overline{u}(r)}{\overline{\rho}_{\mathrm{CL}}\overline{u}_{\mathrm{CL}}}\left(1 - \frac{\overline{u}(r)}{\overline{u}_{\mathrm{CL}}}\right) dr \tag{7}$$

where the centerline mean conditions are used for normalization. The growth of $\delta_\theta(x)$, plotted in Fig. 5, is

well approximated by the linear fit $\delta_\theta/D_j = 0.023\ x/D_j + 0.007$.

The radial location of the inner edge of the shear layer $r_i(x)$ is also relevant to scaling relations that will be developed. Within the extent of the potential core, the inner edge is defined as the interior locus where the magnitude of the mean vorticity equals $0.05U_j/D_j$, that is,

$$|\overline{\omega}(x, r = r_i)| = 0.05\frac{U_j}{D_j}\ ,\ r < D_j/2 \tag{8}$$

Past the potential core, where the annular shear layer has collapsed on itself, we set $r_i = 0$. The axial evolution of r_i is plotted in Fig. 5.

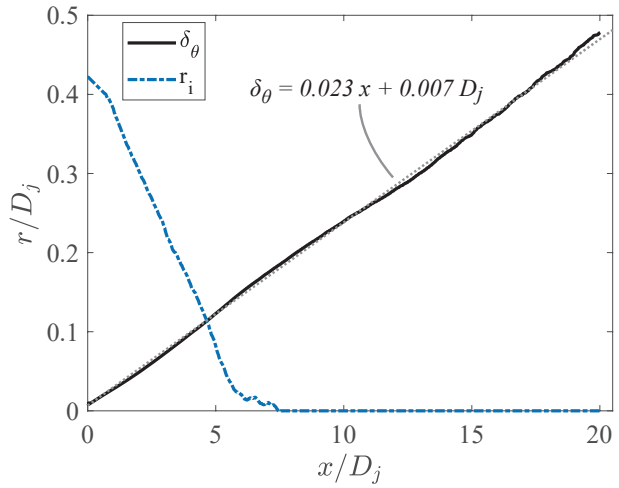

Fig. 5 Axial distributions of momentum thickness δ_θ/D_j (solid black line) and inner edge of shear layer r_i/D_j (dashed blue line). Dotted line indicates linear fit.

B. Reynolds Stress

Isocontours of the normalized Reynolds stress magnitude g/U_j^2 are plotted in Fig. 6. The location of the SPS is included in the figure. The distribution of g/U_j^2 creates two distinct lobes that reach a minimum separation around $x/D_j = 9$. Per its definition, the SPS is the locus of the radial maximum of the Reynolds stress. This places the surface very close to the nozzle lipline ($r/D_j = 0.5$) until $x/D_j = 11$. Downstream of this station, the SPS expands at an angle of approximately 4° with respect to the jet axis. The maximum value of the Reynolds stress is $g/U_j^2 = 0.0089$ and occurs near $x/D_j = 5$.

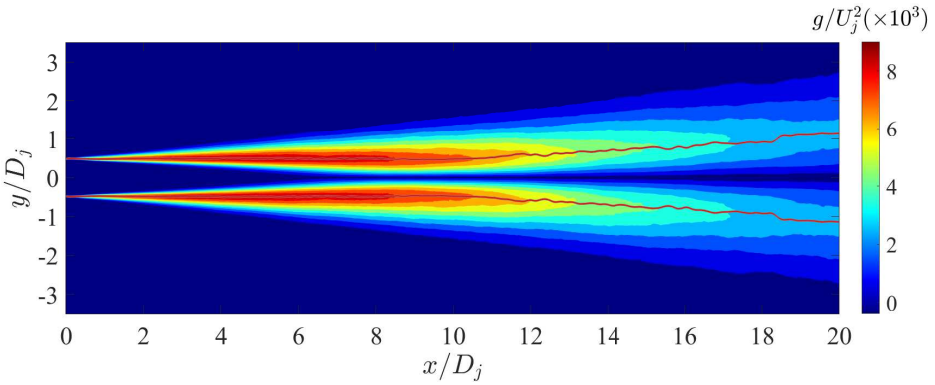

Fig. 6 Isocontours of normalized Reynolds stress magnitude g/U_j^2. Red line: SPS.

C. Convective Velocity

The $x-r$ distribution of the convective velocity U_{c_p} calculated from space-time correlations of the pressure fluctuation is plotted in Fig. 7. Two distinct regions are noted: an inner region, encompassing the jet flow, where U_{c_p} generally follows the trend of the mean axial velocity, and an outer region, near the edge of the jet and beyond, where U_{c_p} rapidly increases to supersonic values indicative of the acoustic field. The radiator surface, depicted by the white line, is located at this transition region between hydrodynamic and acoustic fields. Its growth is nearly linear at an angle of 9° relative to the jet centerline. The SPS is included in the plot for completeness. The trends can be further quantified by plotting the radial distributions of U_{c_p} and $\overline{u}$ at $x/D_j = 5$ in Fig. 8. The potential core is manifested by the flat regions of the profiles near $r = 0$. Starting from the jet centerline, U_{c_p} initially follows the trend of the mean velocity, reaches a minimum, and then starts rising within the rotational region of the jet. This reversal has also been seen in earlier LES of a single-stream jet [41]. The radiator surface is located slightly outwards of the reversal, where U_{c_p} matches that on the SPS. With further increase of the radius, U_{c_p} increases rapidly and attains large values in the acoustic field. The very large, supersonic values of U_{c_p} at large radius represent the trace along x of acoustic waves propagating at large angles with respect to the downstream direction.

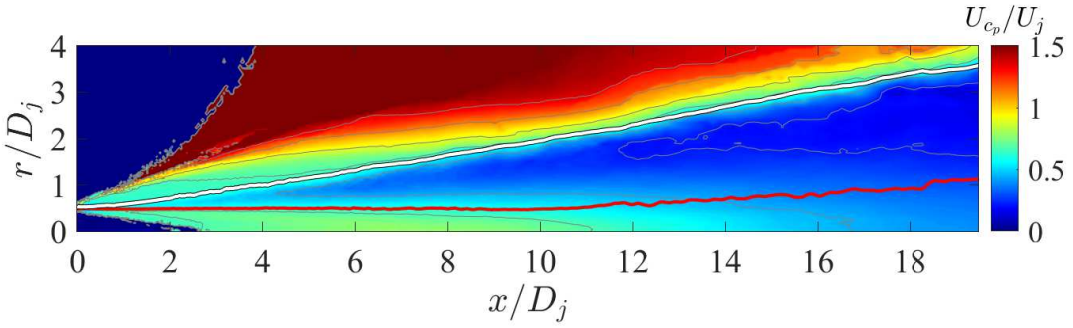

Fig. 7 Isocontours of normalized convective velocity U_{c_p}/U_j on a meridional plane. Red line: SPS. White line: radiator surface.

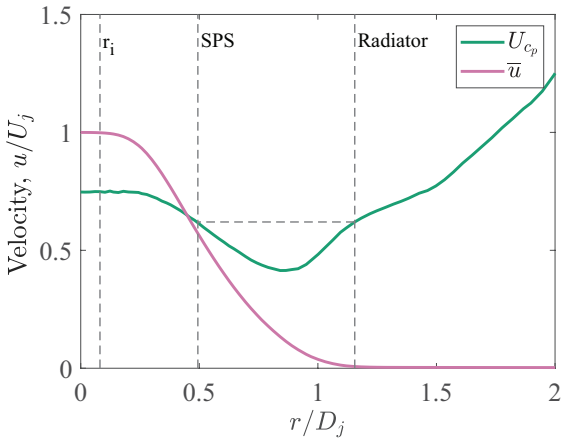

Fig. 8 Radial distributions of U_{c_p} and $\overline{u}$ at x/D_j=5. By definition, U_{c_p} on the radiator surface equals that on the SPS.

It is instructive to compare the axial distribution of U_{c_p} and the mean axial velocity $\overline{u}$ on the SPS. As seen in Fig. 9, the two distributions are very close, with $\overline{u}$ being about 8% lower for $x/D_j < 10$. This indicates that the convective velocity can be approximated well by the axial mean velocity on the SPS [6]. Within the potential core, the convective velocity is near $U_{c_p} = 0.6U_j$. For completeness, the figure includes the convective velocity U_{c_u}, which is based on space-time correlations of u'. The distributions of U_{c_u} and U_{c_p} are practically identical. The three curves of Fig. 9 show that, in the region of the most energetic eddies represented by the SPS, the axial transport of velocity and pressure fluctuations involves the same mechanism of convection by the local mean velocity. This is not true in other regions of the jet where significant differences can be found between U_{c_u} and U_{c_p}.

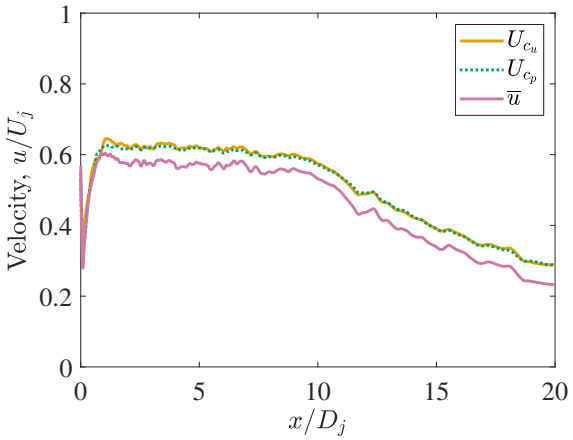

Fig. 9 Axial distributions of U_{c_p}, U_{c_u}, and $\overline{u}$ on the SPS.

VI. Longitudinal Correlations

A. Two-Dimensional Correlations

Correlations on a meridional plane can give insight on the structure of turbulence and resulting acoustic field [21]. They also help in understanding the length scale distributions presented in the following subsections VI.B and VI.C. Space-time correlations R_{uu} and R_{pp} on a meridional plane are plotted in Fig. 10 for three time separations. The reference point is on the SPS at $x/D_j = 3.0$. The normalized time separations are $\tau U_j/D_j = -1.94$ (top row), 0 (middle row) and 1.94 (bottom row). A vertical dashed line indicates the position that corresponds to a downstream convective velocity $U_c = 0.6U_j$. R_{uu} shows a compact area of correlation, mostly limited to a small positive (red) region that travels along the SPS and a negative (blue) oblong region along the radiator surface. On the other hand, R_{pp} has a wide structure of radially-oriented lobes extending from the centerline well into the acoustic field; the main structure comprises a positive lobe (red) flanked by strong negative lobes (blue), resembling a hydrodynamic pressure wave. The structures of R_{uu} and R_{pp} travel at similar convective velocities, but the former is slightly slower and the latter slightly faster than $0.6U_j$.

We now examine the evolution of R_{uu} and R_{pp} with the reference point on the SPS at $x = 7.5D_j$, near the end of the potential core. Figure 11 displays the resulting correlations at time separations $\tau U_j/D_j = -3.49$ (top row), 0 (middle row) and 3.49 (bottom row). The time progression of R_{uu} shows a compact structure of positive correlation traveling along the SPS. The effects of that structure are felt above the radiator surface as a region of negative correlation. At $\tau = 0$, the peak of the negative correlation is -0.24. The limited

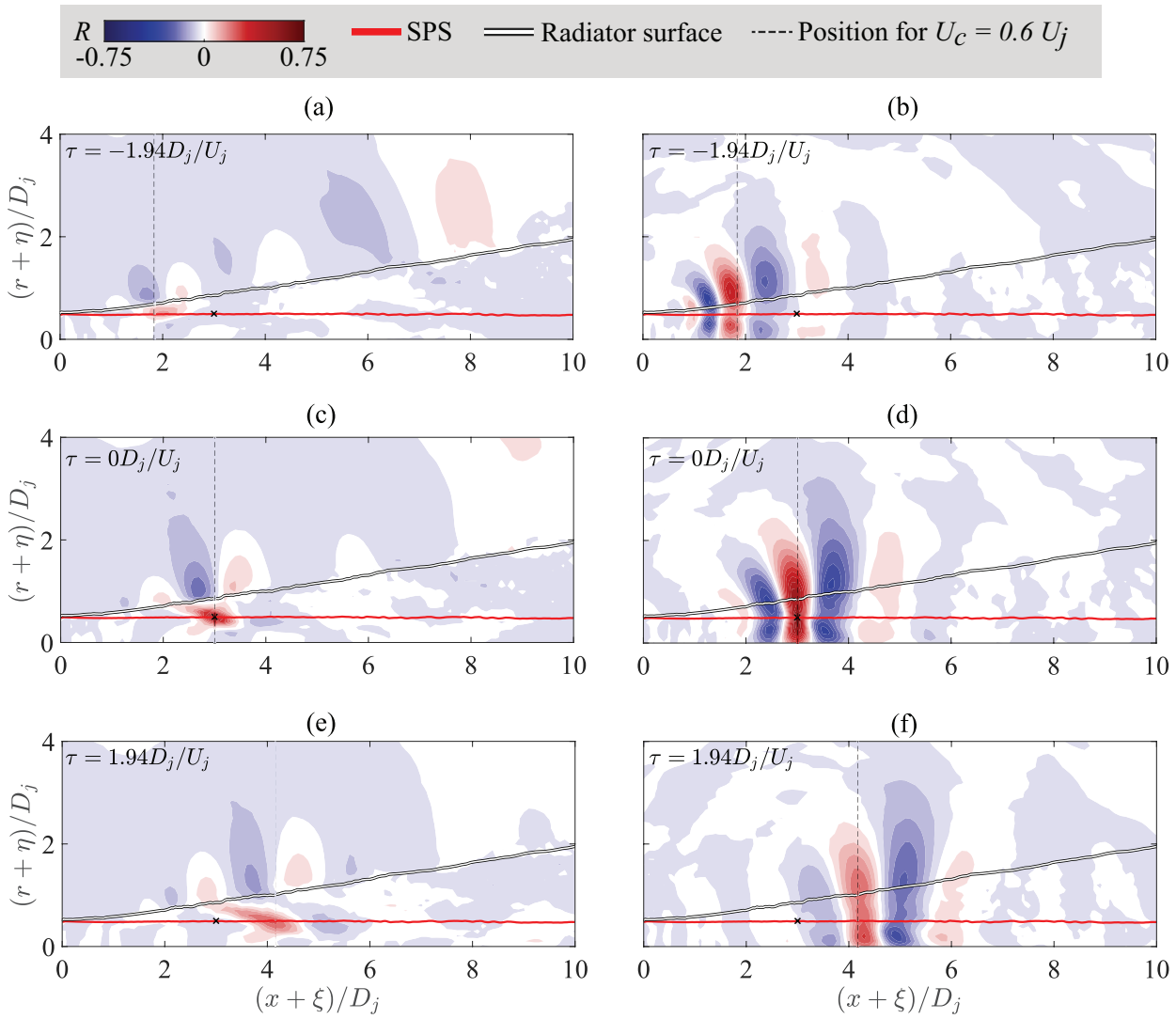

Fig. 10 Contours of R_{uu} (left column) and R_{pp} (right column) with reference point on SPS at $(x,r) = (3, 0.5)D_j$ for three time separations.

size of the positive structure indicates that the u' correlations capture the local but not global effects of the convecting eddies. The axial velocity fluctuation thus becomes decorrelated as we move from the SPS to the outer edge of the jet. This explains the region of low correlation between positive and negative structures in Fig. 11(a,c,d).

The time progression of R_{pp} is seen in Fig. 11(b,d,f). A wavepacket-like structure is evident for all the time separations. At zero time separation, in Fig. 11(d), a region of strong positive correlation emanates as a radial beam from the reference point to all across the jet, from the centerline to well outside the radiator surface. It is evident how the footprint of the large-scale structures is imprinted on the radiator surface. For negative and positive time separations, in Figs. 11(b,f), similar but weaker structures are seen, with a rapid

decorrelation for $\tau > 0$. The latter may be explained by the breakdown of the shear-layer structures after the end of the potential core [42]. It is notable that the R_{pp} correlations structures convect fairly uniformly with a speed near $0.6U_j$, while the R_{uu} structures are stretched and their convective speed depends on radial location.

The differences in location, shape, and convective velocity of the features of R_{uu} and R_{pp} in Figs. 10 and 11 suggest that the two correlations portray events of different nature. The u'-based correlations reflect compact, localized turbulence events that travel along the SPS. The p'-based correlations appear to reflect interactions of eddies with the potential flow around them, namely the ambient air and the potential core, which result in large regions of influence. Consequently, pressure-based scales may not capture local events as accurately as velocity-based scales.

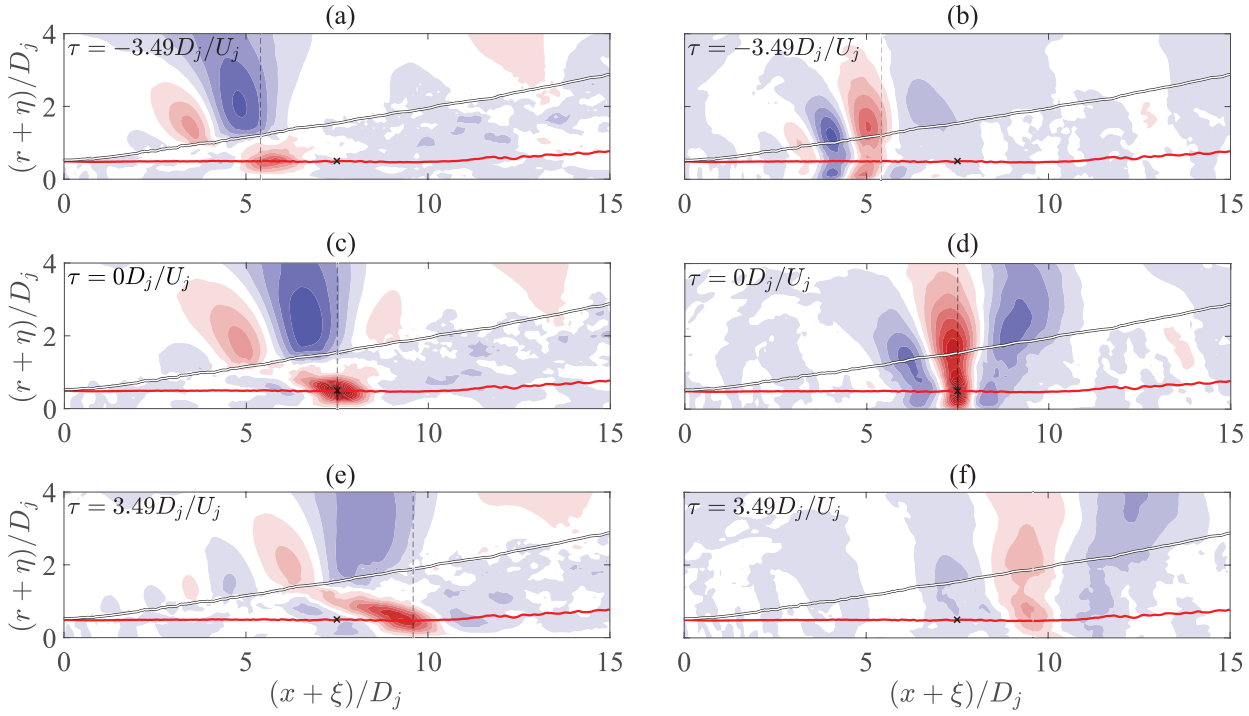

Fig. 11 Contours of R_{uu} (left column) and R_{pp} (right column) with reference point on SPS at $(x,r) = (7.5, 0.5)D_j$ for three time separations. Legend is the same as for Fig. 10.

B. Fixed-Frame Length Scales

The distributions of fixed-frame length scales defined in Section III are now presented. Isocontours of normalized length scales based on axial velocity fluctuation, L_u/D_j, and on pressure fluctuation, L_p/D_j, are plotted in Fig. 12. The radiator surface marks the end of the vortical region, inside of which the scales L

generally follow the axial growth of the momentum thickness. At a given axial location and going outwards from the inner edge of the shear layer r_i, L_u increases, reaches a local maximum within the jet, then decreases to a local minimum at the edge of the jet. Outside the jet, L_u rises to high values. The local radial minimum of L_u follows closely the radiator surface. This suggests a loss of coherence of velocity-based events near the edge of the jet. Near the SPS, L_u experiences the strongest radial variation within the jet flow. In Fig. 12(b) L_p does not have a local maximum inside the jet in the radial direction. Instead, it is strictly increasing until reaching a maximum around one nozzle diameter outwards from the radiator surface. Its maximum radial gradient is found near the radiator surface.

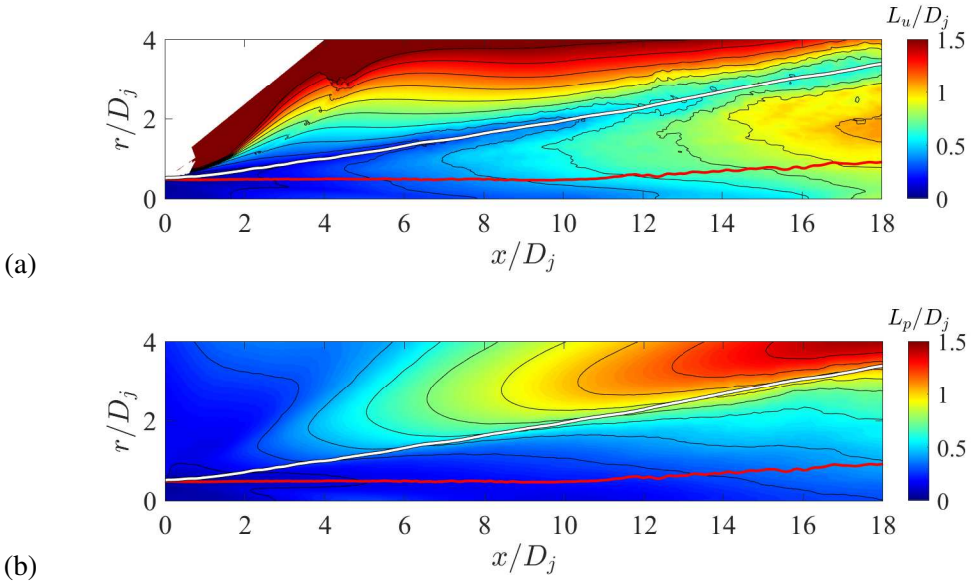

Fig. 12 Isocontours of normalized length scales (a) L_u/D_j and (b) L_p/D_j. Red line: SPS. White line: radiator surface.

The radial trends of Fig. 12 are interpreted as follows. The inner vortical region of the jet, marked by the SPS, contains the main events of mixing and momentum transport of the mixing layer, see Eq. (6). That region encompasses the largest scales of turbulence and, through energy cascade, small scales as well. The combination of large and small scales drives the value of the length scale L below the actual length of the large scales [12]. As one leaves the SPS towards higher radial locations with lower vorticity, the effects of small eddies are lost faster than those of large eddies, resulting in the increase of scales versus radius seen in Figs. 12. It appears that the pressure-based scales grow radially due to this effect until peaking beyond the radiator surface, into the linear field. Thus, that region of radial maxima is due to the footprint of the large-scale vortical structures inside the jet [43, 44]. The velocity-based scales have a different behavior,

whereby they capture the extent of the eddies themselves but not their footprint away from them. As one approaches the outer edge of the jet, the velocity fluctuations disassociate from the core vortical region and become influenced by a combination of acoustic effects and small eddies of secondary acoustic relevance. This complex combination of influences causes the "valley" of low length scale L_u at the edge of the jet seen in Fig. 12(a). This observation is supported by the recent work of Camussi and Bogey [45] on this same jet, which found that the region of the vortical field near the edge of the jet shows high values of intermittency, and thus incoherent behavior. Further away from the jet edge, the acoustic perturbations start to dominate and cause the increase in length scale in the near-acoustic region.

To further quantify the connection between events on the SPS and radiator surface, the axial distributions of length scales L_u and L_p on these surfaces are plotted in Fig. 13. All the curves exhibit a substantially linear growth along the first 15 jet diameters. In addition, the length scales on the SPS acquire a higher value when calculated from velocity fluctuation than from pressure fluctuation. This result challenges the intuitive prediction that velocity scales would be lower due to a richer content of high frequencies, and therefore smaller scales [43]. However, this difference is likely to result from the specific definition of length scale used, based on Eq. (3), where only positive values of the correlation function are considered. Indeed, the correlations in Figs. 10 and 11 at $\tau = 0$ show strong negative lobes of R_{pp} upstream and downstream from the reference point. Therefore, if negative values of correlations were to be considered when defining the axial span of turbulence events, the pressure-based length scale would be longer than the velocity-based scale. Comparing scales based on the same variable, it is evident that those on the radiator surface are consistently larger than those on the SPS, with the pressure-based scale exhibiting the strongest increase in this regard. These results suggest that the signature of the eddies on the radiator surface is more coherent than the effect of the eddies in the vortical field. They are in line with the findings of Arndt *et al.* [46] that the pressure signal measured at the outer edge of a jet mixing layer is dominated by the large-scale structure of the turbulent flow and is correlated over longer distances than the underlying velocity fluctuations.

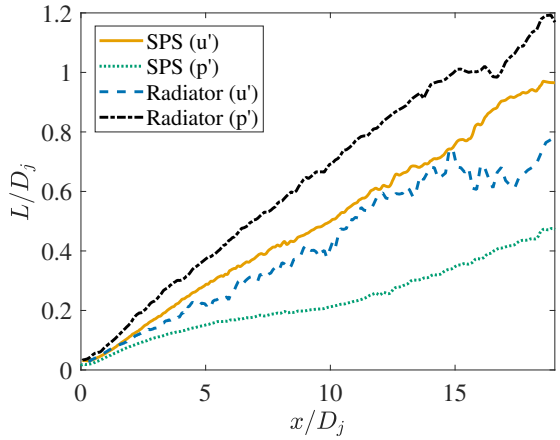

Fig. 13 Axial distribution of the correlation scales L on the relevant surfaces. Orange solid line: L_u on SPS. Blue dashed line: L_u on the radiator surface. Green dotted line: L_p on SPS. Black line dash-dot: L_p on the radiator surface.

To examine the radial evolution of the correlation scales, they are plotted in the "similarity" form $L/\delta_\theta(x)$ versus $(r - r_i(x))/\delta_\theta(x)$. This form represents the expectation that the correlation scale grows with the momentum thickness δ_θ. The radial variations of the correlation scales at eight axial stations, from $x/D_j = 1$ to 15, are shown in Fig. 14(a) for L_u and Fig. 14(b) for L_p. The locations of the centerline, SPS, and radiator surface are marked. The similarity form leads to a fair collapse of the curves, particularly for axial locations $x/D_j \geq 3$ for L_u and $x/D_j \geq 5$ for L_p. The length scales at $x/D_j = 1$ and $x/D_j = 3$ acquire high values near the centerline, possibly indicating the influence of coherent waves within the potential core. Overall, at all axial stations, common trends are found between the SPS (marked in black squares) and the radiator surface (blue circles) even though the trends differ between L_u and L_p. At high radii of $(r-r_i)/\delta_\theta \geq 12$, the curves diverge as a result of the acoustic propagation in a variety of directions depending on the axial position considered. The results in Fig. 14 are in agreement with the those by Fleury *et. al.* [14] and Proença *et al.* [13], in which fixed-frame, u'-based correlation scales along the centerline and lipline grow according to the shear-layer width. This consistent scale growth is generalized here for all relevant axial and radial locations, and for both velocity- and pressure-based scales.

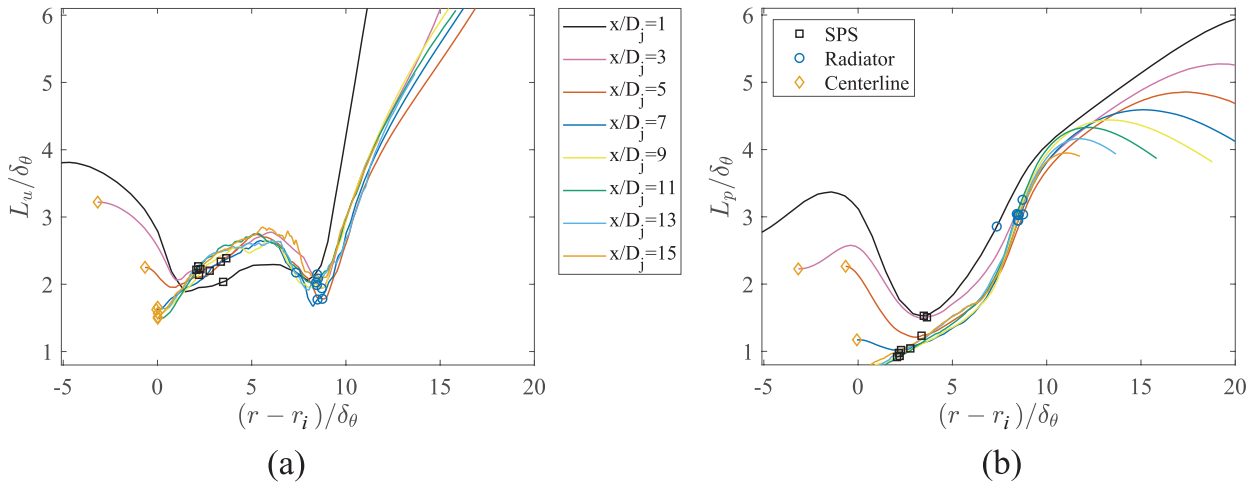

Fig. 14 Plots of normalized length scales L/δ_θ versus normalized radius $(r-r_i)/\delta_\theta$, (a) based on axial velocity, (b) based on pressure. Legend applies to both subfigures.

C. Moving-Frame Length Scales

The distributions of the normalized moving-frame length scales based on axial velocity fluctuation $\widehat{L}_u/D_j$ and pressure fluctuation $\widehat{L}_p/D_j$ are presented in Fig. 15. The trends are somewhat similar to those seen for the fixed-frame scales in Fig. 12. With regards to the velocity-based scales, a notable difference is that the radial maxima of $\widehat{L}_u$ inside the vortical field in Fig. 15(a) are more localized and occur inward, closer to the SPS, relative to those of L_u in Fig. 12 (a). This difference can be explained by examining the convection of the structures in Figs. 10 and 11, where the positive structure of R_{uu} rotates counter-clockwise as a result of the convective velocity decreasing with radius within the vortical region. High convective velocity near the jet axis elongates the lifespan of the turbulence, which is reflected by the radial maxima of $\widehat{L}_u$ near the SPS. As with the fixed-frame scale distribution of Fig. 12 (a), $\widehat{L}_u$ reaches minimum value near the location of the radiator surface. The pressure-based scale $\widehat{L}_p$ follows the same general trends as $\widehat{L}_u$ but with lower values within the vortical region and a weak maximum slightly outside the SPS. Immediately outside the radiator surface, $\widehat{L}_p$ rises rapidly to high values.

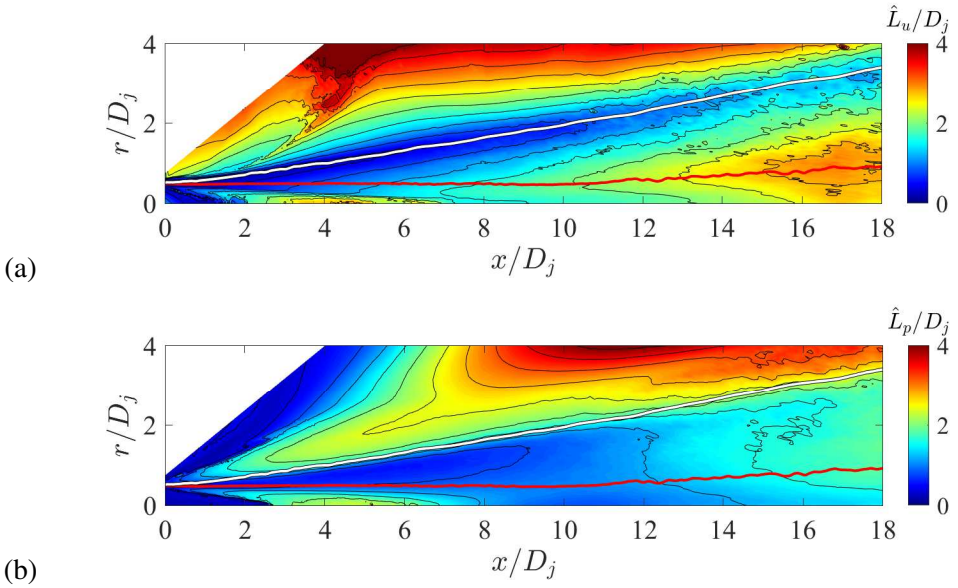

Fig. 15 Isocontours of normalized length scales (a) $\widehat{L}_u/D_j$ and (b) $\widehat{L}_p/D_j$. Red line: SPS. White line: radiator surface.

The axial distributions of the moving-frame length scales on the SPS and radiator surface are plotted in Fig. 16. Contrary to the fixed-frame length scales, where all curves exhibit a linear growth, here only those based on axial velocity fluctuation increase linearly on the SPS. The pressure-based length scale $\widehat{L}_p$ rises rapidly within the first few jet diameters, reaches an apparent plateau, then resumes growth at a lower rate. On the radiator surface, it increases linearly at a fast rate up to $x/D_j \approx 2.5$, reaches a plateau for $2.5 \leq x/D_j \leq 7.5$, then grows at a rate similar to that of $\widehat{L}_u$. The difference in the trends of $\widehat{L}_u$ and $\widehat{L}_p$ is in line with the observations made in Section VI.A, where it is discussed that $\widehat{L}_u$ follows the growth of the vortical region, while $\widehat{L}_p$ appears affected by large-scale events that result from interactions of eddies with the potential flow surrounding them. Thus, $\widehat{L}_p$ grows faster than the shear layer in the initial few diameters of the jet. The nature of this phenomenon remains under investigation.

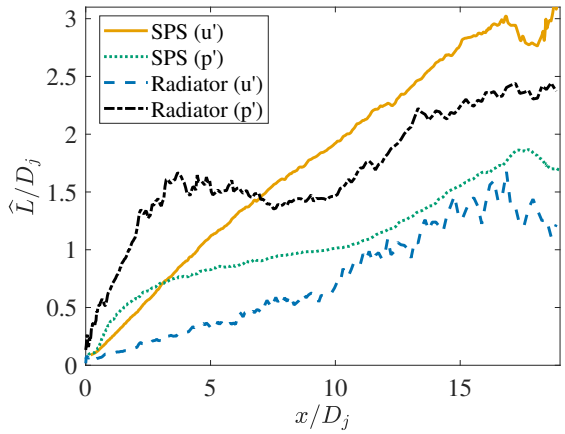

Fig. 16 Axial distribution of length scales $\widehat{L}$ on the relevant surfaces. Orange solid line: $\widehat{L}_u$ on SPS. Blue dashed line: L_u on the radiator surface. Green dotted line: $\widehat{L}_p$ on the SPS. Black line dash-dot: $\widehat{L}_p$ on the radiator surface.

The radial variations of $\widehat{L}_u$ and $\widehat{L}_p$ are plotted in Fig. 17 using a normalization based on δ_θ as in Fig. 14. The curves at locations past the end of the potential core tend to collapse well. The curves at early axial locations also are very close to each other in the case of $\widehat{L}_u$ in Fig. 17(a), which shows an approximately self-similar behaviour in agreement with the results by Proença *et al.* [13]. In contrast to $\widehat{L}_u$, the scales $\widehat{L}_p$ in Fig. 17(b) grow rapidly near the nozzle exit and do not exhibit self-similar behavior.

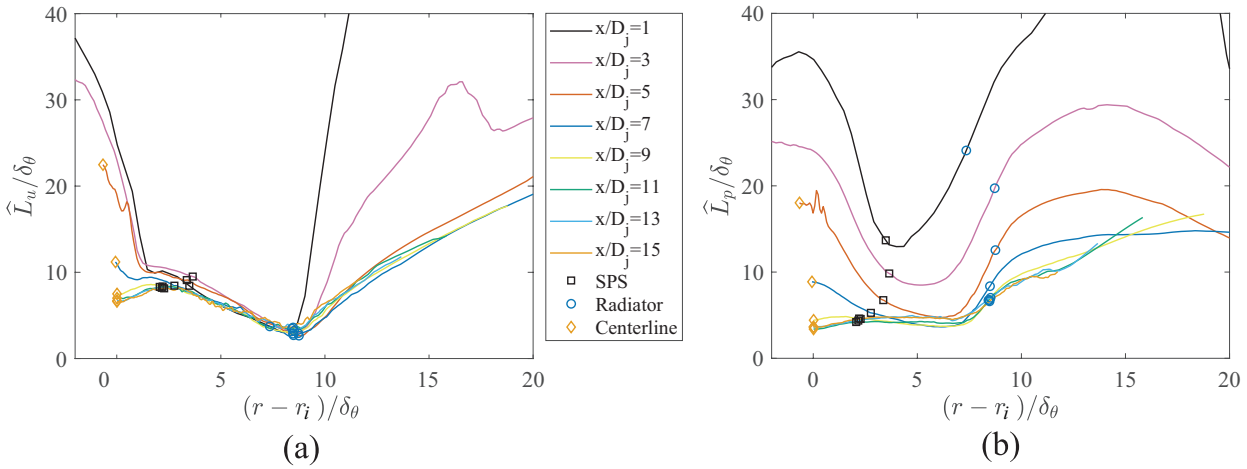

Fig. 17 Plots of normalized moving-frame length scales $\widehat{L}/\delta_\theta$ versus similarity coordinate $(r-r_i)/\delta_\theta$, (a) based on axial velocity; (b) based on pressure. Legend applies to both subfigures.

VII. Azimuthal Correlations

A. Modal Components

The azimuthal composition of the flow is studied by examining the radial variations of the energy of its Fourier modes m. The energy of the first five Fourier modes that compose the u' and p' fluctuations is shown in Fig. 18. These distributions do not significantly depend on their axial location, so the results are only shown for $x/D_j = 7.5$. The modal energy distribution based on velocity fluctuation in Fig. 18(a) shows that the vortical region is dominated by modes $m = 2, 3, 4$, whose contributions peak near the location of the SPS. Lower modes such as $m = 0, 1$ contain lower energy inside the vortical region but dominate the linear field past the radiator surface. On the other hand, the modal energies based on pressure fluctuation in Fig. 18(b) have fairly constant levels between the SPS and the radiator surface, with mode $m = 1$ accounting for 33% of the total modal power. Going from the vortical to the linear field, the contributions of modes 0 and 1 rise and peak at distances $1.0D_j$ and $0.3D_j$ from the radiator surface, respectively. In that region, the two modes represent about 80% of the total power. Continuing outwards, the energy of those modes decreases and all modes reach levels between 8% and 28%. This radial variation is consistent with the radiation pattern observed in turbulent jets, where low modes dominate at shallow angles from the jet axis, and all modes have similar energy levels radiating perpendicularly to the jet axis [47].

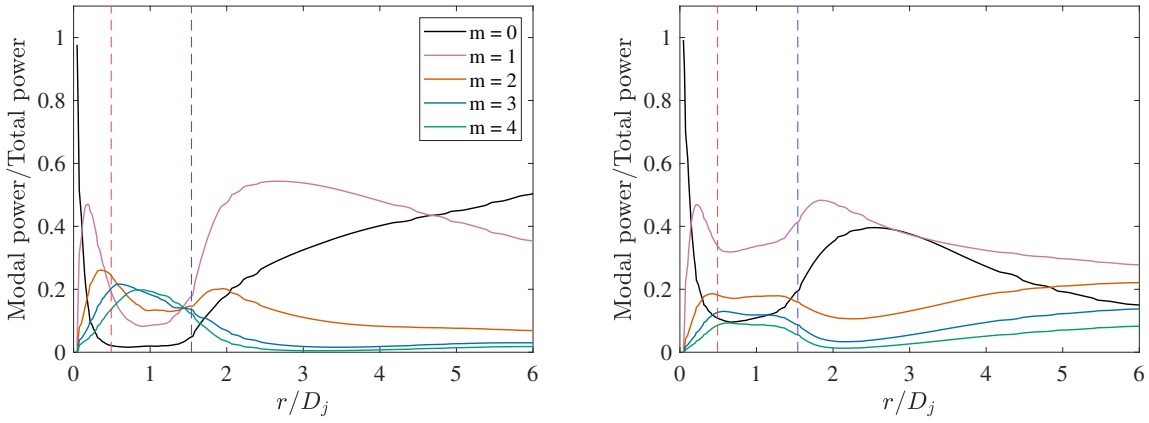

Fig. 18 Radial distribution of modal powers on $x = 7.5D_j$ for the first five modes; (a) based on axial velocity, (b) based on pressure. The vertical lines mark the locations of the SPS (red) and the radiator surface (blue).

B. Cross-Sectional Correlations

Two-dimensional correlations performed on a cross section of the jet at $x/D_j = 7.5$ are represented in Fig. 19. The reference point is located on the SPS and marked by a white cross. The displacement in the z and y directions are denoted ζ and ψ, respectively. Similarly to the longitudinal correlations presented in Subsection VI.A, there are notable differences between the distributions of R_{uu} and R_{pp}. The velocity correlations in Fig. 19(a) show a discrete, oblong shape of limited radial and azimuthal extent, flanked by negative sidelobes. The pressure correlations in Fig. 19(b) exhibit a wider azimuthal extent that remains roughly constant within the vortical field and increases rapidly in the linear field.

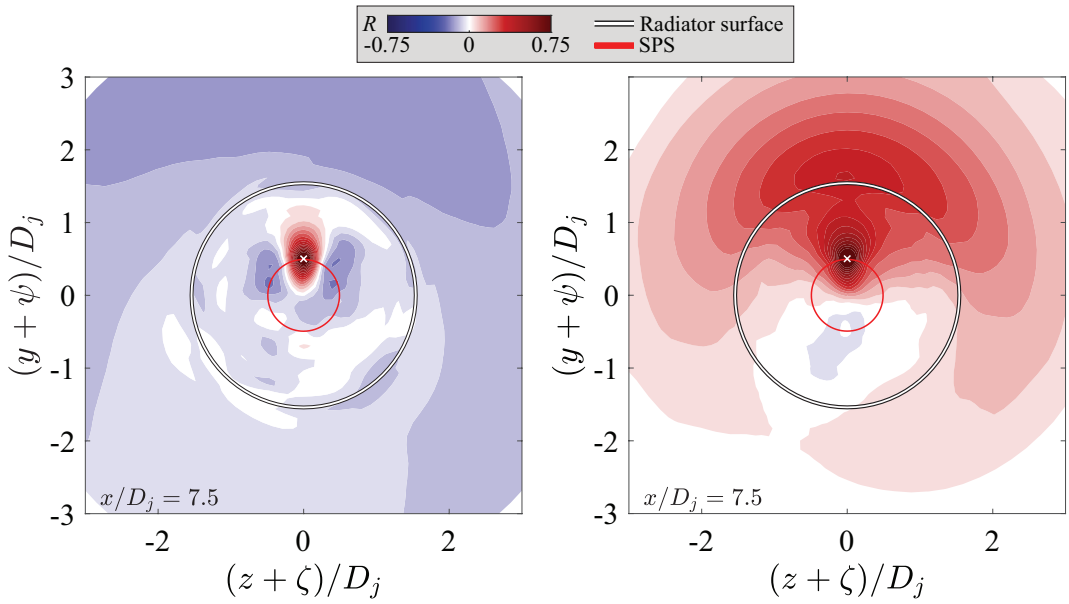

Fig. 19 Contours of (a) R_{uu} and (b) R_{pp} on the cross-sectional plane $x = 7.5D_j$ with reference point on SPS at $\phi = \pi/2$ (white cross). Time shift is zero.

C. Azimuthal Scales

Isocontours of azimuthal scales based on axial velocity and pressure fluctuations are plotted in Fig. 20. By definition, there is full azimuthal coherence in the vicinity of the centerline as $r \to 0$. For both distributions, the azimuthal scale reaches a minimum of around 15° for Φ_u and 25° for Φ_p inside the vortical layer. With increasing radius, the azimuthal scale rises and becomes large in the acoustic near field. This rise starts earlier for Φ_p. The distributions in Fig. 20 reflect a similar behavior to the fixed-frame length scales L_u and L_p, plotted in Fig. 12, divided by the radius r.

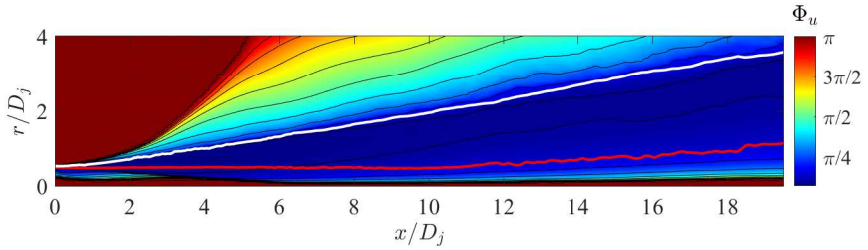

(a)

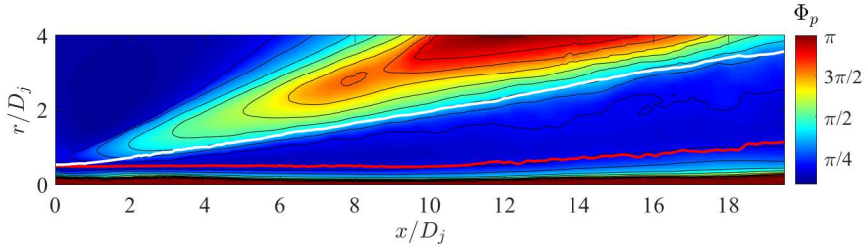

(b)

Fig. 20 Isocontours of normalized azimuthal scales (a) Φ_u and (b) Φ_p, units are radians. Red line: SPS. White line: radiator surface.

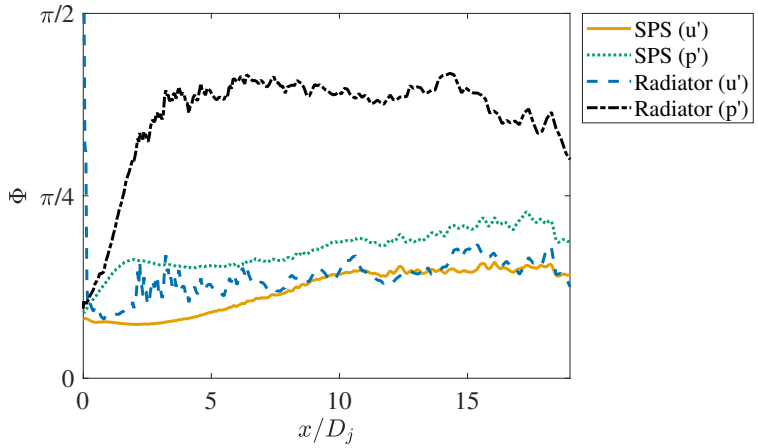

Fig. 21 Axial distribution of azimuthal scales Φ on the relevant surfaces. Orange solid line: Φ_u on SPS. Blue dashed line: Φ_u on the radiator surface. Green dotted line: Φ_p on the SPS. Black line dash-dot: Φ_p on the radiator surface.

The axial distributions of Φ_u and Φ_p on the SPS and radiator surface are plotted in Fig. 21. All curves display an initial growth followed by saturation. The saturation is consistent with the circumferential length scale and the radius of the surface both growing linearly. The pressure-based azimuthal scales Φ_p display a faster initial growth than the velocity-based scales Φ_u. On the radiator surface, Φ_p show the strongest correlation, which is consistent with the cross-sectional results in Fig. 19(b). They grow rapidly within the

first three jet diameters, then saturate at approximately $\pi/3$. Radial profiles of Φ_u and Φ_p are plotted in Fig. 22 as a function of $(r - r_i)/\delta_\theta$ and for several axial stations. Except for the region very near the nozzle exit ($xod \leq 1$) the profiles for each scale collapse fairly well within the radiator surface.

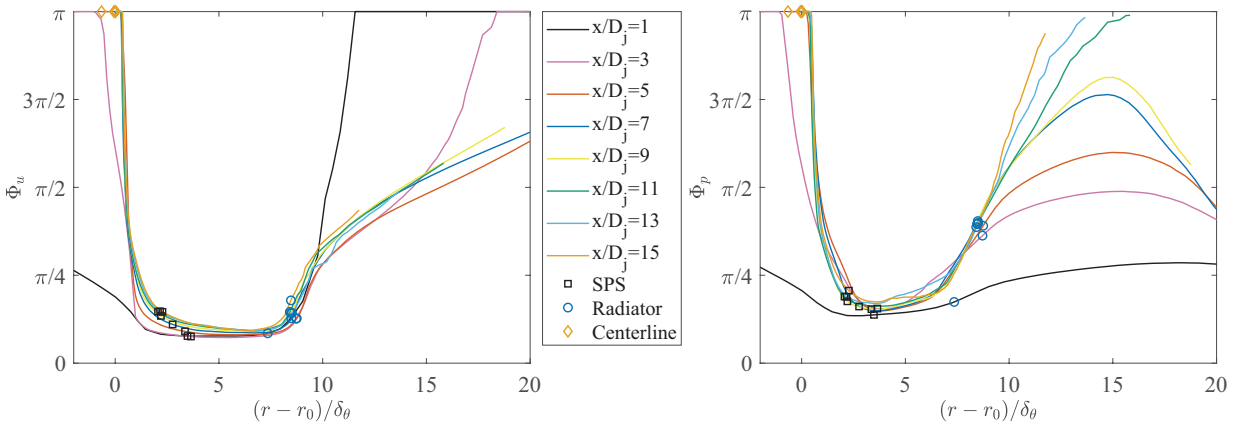

Fig. 22 Azimuthal scales Φ versus similarity coordinate $(r - r_i)/\delta_\theta$, (a) based on axial velocity; (b) based on pressure. Legend applies to both subfigures.

VIII. Modeling Based on the Time-Averaged Flow

The previous sections used the LES flow field to gain insight into the correlations between the vortical and the near-acoustic fields. The radiator surface is defined to contain the imprint of turbulent eddies that is crucial for modeling the jet noise source. However, the LES is costly and cannot yet be considered as a design tool. Can the properties on the radiator surface be informed by the time-averaged solution? This question is addressed here at a preliminary level.

A. RANS-Based Statistics

RANS-based statistics are relevant to the low-cost modeling of the noise source proposed in Ref. [6]. Here we do not use results derived directly from a RANS simulation of the jet, but instead use the statistics of the LES fields to emulate a RANS simulation. While this approach was taken because of a lack of a readily available, equivalent RANS simulation, an advantage of this emulation can be recognized: it allows us to avoid the discrepancies typically obtained by RANS and LES solutions due to the turbulence and subgrid models used. Here, the relations between turbulence structures and their impact on the time-averaged flow thus are evaluated without differences in the mean flow fields. To distinguish our approach from a direct RANS solution we will refer to it as “emulated RANS" and abbreviate it as eRANS.

Comparison of jet flow fields calculated from LES and direct RANS shows similar distributions for mean velocity, turbulent kinetic energy, and Reynolds stress [16, 41]. Importantly, the peak values of turbulent kinetic energy and Reynolds stress are matched well. A consistent trend is that RANS overpredicts by about 10-20% the length of the potential core relative to the LES. The same observation applies when comparing RANS to experiments [48] and is a well-known shortcoming of RANS closure models for free shear flows [49]. Because the errors are systematic, they can be accounted for in jet noise prediction methodologies [12, 48]. With regards to the eRANS results to be presented here, it is expected that they will capture more faithfully the real mean flow than a direct RANS simulation would. However, a direct RANS solution could be scaled, if necessary, to filter out the effects of the over-predicted potential core length.

The eRANS flow field comprises the mean velocity vector, mean density, turbulent kinetic energy k and viscous dissipation ϵ. The principal component of the Reynolds stress, the analogue to Eq. (6), is modeled as

$$g \;=\; \nu_T \left| \frac{\partial \overline{u}}{\partial r} \right| \tag{9}$$

where the turbulent viscosity ν_T is given by the dimensional construct

$$\nu_T \;=\; C_\mu \frac{k^2}{\epsilon} \tag{10}$$

The coefficient C_μ was set here at the value of 0.067, as will be discussed in Subsection VIII.C.

Relying again on a dimensional construct, the eRANS-based length scale is

$$L = C_L \frac{k^{3/2}}{\epsilon} \tag{11}$$

A related azimuthal scale is based on the above length scale divided by the radial coordinate r of the relevant surface:

$$\Phi = C_\Phi \frac{k^{3/2}}{\epsilon\, r} \tag{12}$$

In the above relations, C_L and C_Φ are coefficients determined empirically for the LES; k and ϵ are evaluated on the SPS.

LES allows for the direct computation of the turbulent kinetic energy. It does not give directly the viscous dissipation because the energy dissipation combines viscous and filtering effects [35]. The actual viscous

dissipation ϵ must be computed from the budget of turbulent kinetic energy. Following Darisse *et al.* [50], the dissipation in a turbulent axisymmetric jet is computed as

$$\epsilon = -\left[\bar{u}\frac{\partial k}{\partial x} + \bar{v}\frac{\partial k}{\partial r}\right] - \left[\overline{u'^2}\frac{\partial \bar{u}}{\partial x} + \overline{v'^2}\frac{\partial \bar{v}}{\partial r} + \overline{w'^2}\frac{\bar{v}}{r} + \overline{u'v'}\left(\frac{\partial \overline{v}}{\partial x} + \frac{\partial \overline{u}}{\partial r}\right)\right] - \left[\frac{\partial \overline{\kappa u'}}{\partial x} + \frac{1}{r}\frac{\partial\left(r\overline{\kappa v'}\right)}{\partial r}\right] - \frac{1}{\rho}\left[\frac{\partial \overline{p'u'}}{\partial x} + \frac{1}{r}\frac{\partial\left(r\overline{p'v'}\right)}{\partial r}\right] \quad (13)$$

where $\kappa = (u'^2 + v'^2 + w'^2)/2$ is the instantaneous turbulent kinetic energy. We identify the first term (in brackets) as the advection, the second one as the production, the third one as the turbulent transport, and the fourth one as the transport by pressure fluctuations.

B. Radiator Surface

As the radiator surface marks the transition between the vortical and the linear fields, it is natural to seek a criterion for its location based on the mean vorticity $\overline{\omega}$. The following criterion

$$|\overline{\omega}|\frac{D_j}{U_j} = C_\omega$$

is proposed, with C_ω chosen to get a match with the radiator surface defined in Section IV and displayed in Fig. 4. An excellent agreement is found for $C_\omega = 0.03$ in Fig. 23. Note that the location of the eRANS-based radiator surface is fairly insensitive to C_ω as long as C_ω is small. Varying C_ω from 0.01 to 0.10, for instance, results in a change in the angle of radiator surface of $\pm 1^\circ$ around the actual angle of 9°.

C. Convective Velocity

Recall that, by definition, the convective velocity on the radiator surface equals than on the SPS. The distribution of the eRANS-based Reynolds-stress field defined by Eq. (9) is practically identical to that given by LES using Eq. (6), displayed in Fig. 6, with $C_\mu = 0.067$ in Eq. 10. This value is somewhat lower than the commonly used $C_\mu = 0.09$, but the value of C_μ does not affect the conclusions that follow. Given the strong similarity of the eRANS- and LES-based Reynolds stress fields, the eRANS-based SPS is very close to the LES-based SPS. Following the concept introduced in Ref. [6], the eRANS-based convective velocity

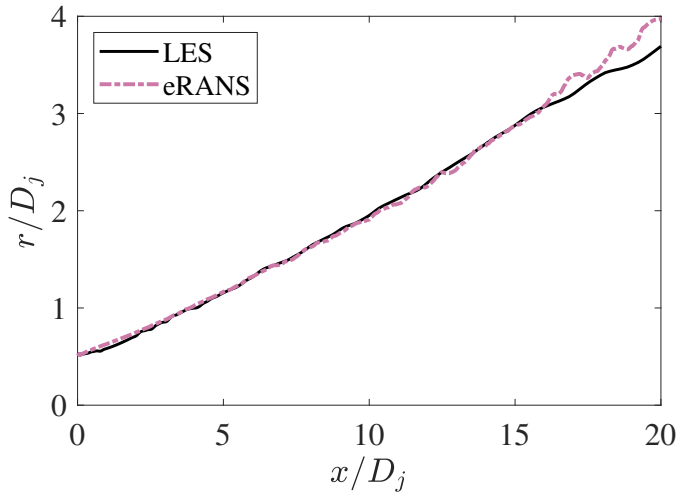

Fig. 23 Approximation of the radiator surface using the criterion $|\overline{\omega}|D_j/U_j = 0.03$.

is modeled as the mean axial velocity on the SPS, that is,

$$U_{c,\text{eRANS}} = \overline{u}(x, r = r_{\text{SPS}}) \tag{14}$$

where r_{SPS} denotes the radial location of the eRANS-based SPS. As shown in Fig. 24, a good agreement is obtained between the axial distributions of U_{c_p} on the radiator surface, derived from the space-time correlations of p', and of $U_{c,\text{eRANS}}$. Note that this agreement does not involve any tunable parameters.

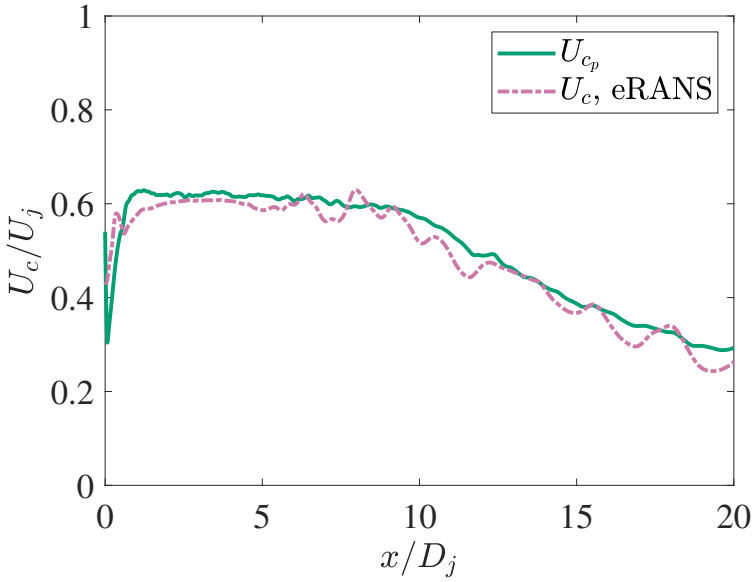

Fig. 24 Comparison of LES- and eRANS-derived convective velocities on the radiator surface.

D. Length Scales

eRANS-based length scales are evaluated using Eq. (11) on the eRANS-derived SPS. They are compared with the LES-derived scales, based on p', on the radiator surface in Fig. 25. The fixed-frame scale L_p, which displays a linear growth, is matched well by the eRANS scale with $C_L = 0.76$. The trend of the moving-scale scale $\widehat{L}_p$ is more complex, as discussed in Subsection VI.C, and thus not amenable to simple scaling. The rapid initial rise can be modeled by the eRANS scale with $C_L = 5.65$ up to about $x/D_j = 2.5$. A plateau of $\widehat{L}_p/D_j \approx 1.5$ follows, and an apparently linear growth resumes past the end of the potential core, $x/D_j \geq 7.5$. The latter trend can be matched by the eRANS scale with $C_L = 1.65$. The complex growth for $\widehat{L}_p$ suggests different mechanisms for p' generation in the initial region of the jet and in the region past the end of the potential core. A full understanding of the physics is lacking at this point and will be the topic of future research.

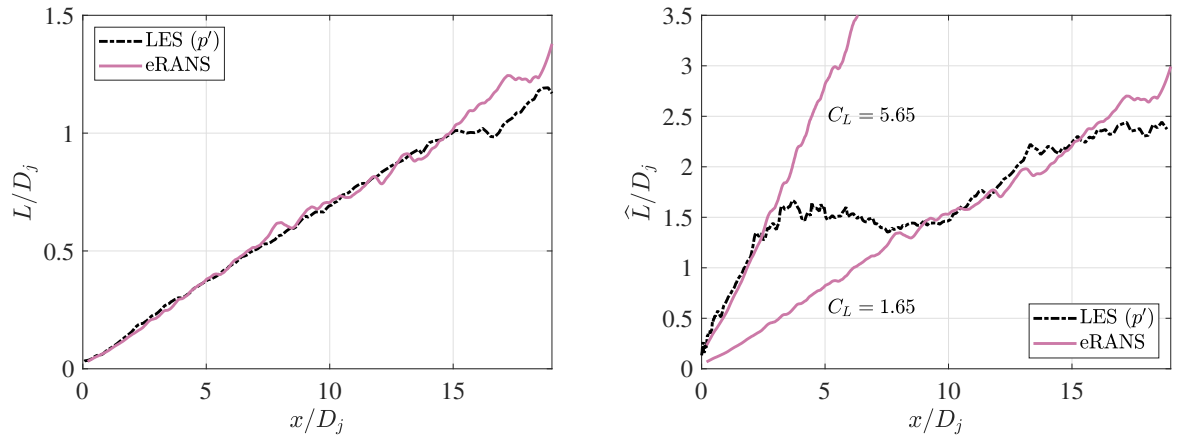

(a) **(b)**

Fig. 25 Fitting of eRANS-based length scales on the radiator surface. (a) Fixed-frame scale with $C_L = 0.76$; (b) moving-frame scale with $C_L = 5.65$ and $C_L = 1.65$ for the initial region and for the region past the potential core, respectively.

E. Azimuthal Scale

The eRANS-based azimuthal scale is calculated from the eRANS length scale divided by the radius of the relevant surface. Here Eq. (12) is evaluated with k and ϵ on the SPS and radius r set to that of the radiator surface. As shown in Fig. 26, the coefficient $C_\Phi = 2.6$ results in a eRANS-based azimuthal scale that provides a fair approximation to the growth and saturation of the LES-derived azimuthal scale based on R_{pp}.

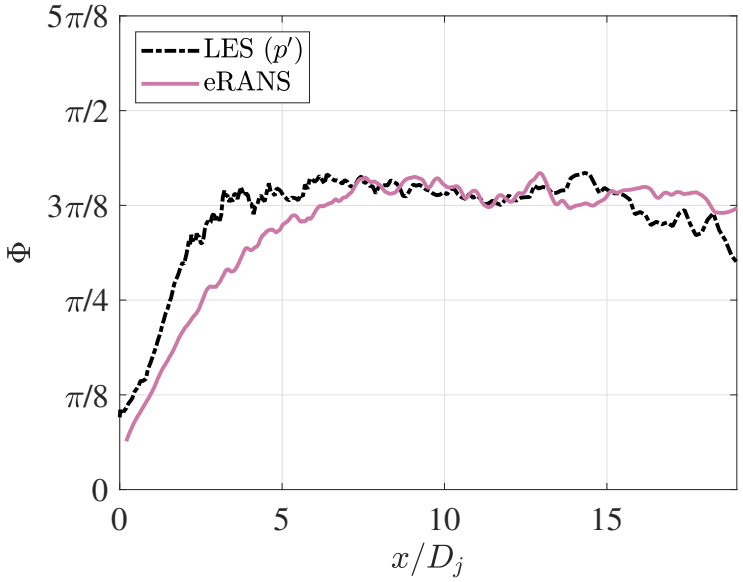

Fig. 26 Fitting of eRANS-based azimuthal scales on the radiator surface with $C_\Phi = 2.60$.

IX. Concluding Remarks

A highly-resolved LES of a Mach 0.9 isothermal turbulent jet is used to investigate the connection between the statistics of the vortical field and its pressure signature on the edge of the jet. The representative locations for those regions are the surface of peak Reynolds stress (SPS) and the radiator surface, respectively. The radiator surface is defined in previous works [17] as the location where the convective velocity equals that on the SPS. Two-point, space-time correlations are used to compute the convective velocity and correlation scales in the axial and azimuthal directions across the vortical and very near fields of the jet. The correlations are based on the axial velocity fluctuation u' and pressure fluctuation p'. In the two cases, two definitions of axial scales are considered, the fixed-frame scale L and the moving-frame scale $\widehat{L}$.

The two-dimensional space-time correlations evaluated along a longitudinal and a cross-sectional plane, for reference points on the SPS, help us to understand the phenomena at play and key differences between velocity and pressure fluctuations. On the radial-axial plane, pressure-based correlations exhibit a wavepacket-like pattern that is coherent radially and travels fairly uniformly with the convective velocity U_c on the SPS. On the contrary, the velocity-based correlation lacks strong radial coherence and its convection is non-uniform, strongly influenced by the local mean-flow velocity. These results suggest that velocity-based correlations capture localized turbulent events, while the pressure-based correlations are dominated by the interaction of large eddies with the surrounding potential flow. Consequently, the axial and radial distributions of the

corresponding length scales follow different trends. The pressure-based correlation scales on the radiator surface are larger than the velocity- or pressure-based scales on the SPS, indicating that fine-scale vortical motions do not significantly imprint the pressure field on the radiator surface. These observations are also applicable to correlations on a cross-sectional plane. There, the velocity-based correlation show events at the SPS have a limited range of effect, while pressure-based correlations have a wide azimuthal range of influence, which grows notably outside the radiator surface.

Regarding the axial trends, the velocity-based length and azimuthal scales increase largely linearly with downstream distance, thus following the spreading of the vortical region. The same holds for the moving-frame length scales based on velocity. However, the moving-frame length scale based on pressure grows rapidly in the first few jet diameters, saturates, then grows slowly. This effect is most notable on the radiator surface. The azimuthal scale based on pressure also rises quickly and then saturates.

The radial variations of fixed-frame length scales collapse well on a single curve when the radial coordinate is offset by the radial location of the inner edge of the shear layer and normalized by the momentum thickness. This works particularly well for axial locations of $x \geq 3D_j$. The same scaling is carried out with moving-frame length scales and azimuthal scales, with equally good results with the exception of moving-frame length scales based on pressure whose growth does not follow that of the momentum thickness. A particularly interesting finding is that the radiator surface passes through a "valley" (local minimum) of velocity-based length scale (fixed or moving-frame), indicating that the velocity fluctuations there are mostly decorrelated from events in the core vortical region.

The potential of extracting relevant velocity and length scales from the time averaged flow field is finally evaluated. LES results are used to emulate a RANS solution (eRANS). The focus is on p'-based scales on the radiator surface. eRANS can predict satisfactorily the convective velocity on the radiator surface without any fitting parameters. The distributions of azimuthal scale and fixed-frame axial length scale are matched approximately by fitting constants to the eRANS-derived scales. The distribution of moving-frame axial length scale is complex and requires a higher level of empiricism. The geometry of the radiator surface can be accurately reproduced using a criterion based on the magnitude of the mean vorticity.

Acknowledgment

We gratefully acknowledge a Balsells Fellowship that partially supported A. Adam. C. Bogey was partially supported by the LABEX CeLyA (ANR-10-LABX-0060/ANR-16-IDEX-0005).

The jet simulations have been performed using HPC resources from PMCS2I (Pôle de Modélisation et de Calcul en Sciences de l'Ingénieur et de l'Information) of École Centrale de Lyon and from IDRIS (Institut du Développement et des Ressources en Informatique Scientifique) under the allocation 2020-2a0204 made by GENCI (Grand Equipement National de Calcul Intensif).

References

[1] Ffowcs Williams, J., and Hawkings, D., "Sound Generation by Turbulence and Surfaces in Arbitrary Motion," *Philosophical Transactions of the Royal Society A*, Vol. 264, No. 1151, 1969, pp. 321–342. https://doi.org/10.1098/rsta.1969.0031.

[2] Pilon, A., and Lyrintzis, A., "Development of an Improved Kirchhoff Method for Jet Aeroacoustics," *AIAA Journal*, Vol. 36, No. 5, 1998, pp. 783–790. https://doi.org/10.2514/2.437.

[3] Papamoschou, D., "Prediction of Jet Noise Shielding," *AIAA Paper 2010-0653*, 2010. https://doi.org/10.2514/6.2010-653.

[4] Piantanida, S., Jaunet, V., Huber, J., Wolf, W., Jordan, P., and Cavalieri, A., "Scattering of Turbulent-Jet Wavepackets by a Swept Trailing Edge," *Journal of the Acoustical Society of America*, Vol. 140, No. 6, 2016, pp. 4350–4359. https://doi.org/10.1121/1.4971425.

[5] Henderson, B., Leib, S., and Wernet, M., "Measurements and Predictions of the Noise from Three-Stream Jets," *AIAA Paper 2015-3120*, 2015. https://doi.org/10.2514/6.2015-3120.

[6] Papamoschou, D., "Modelling of Noise Reduction in Complex Multistream Jets," *Journal of Fluid Mechanics*, Vol. 834, 2018, pp. 555–599. https://doi.org/10.1017/jfm.2017.730.

[7] Papamoschou, D., Johnson, A. D., and Phong, V., "Aeroacoustics of Three-Stream High-Speed Jets from Coaxial and Asymmetric Nozzles," *Journal of Propulsion and Power*, Vol. 30, No. 4, 2014, pp. 1055–1069. https://doi.org/10.2514/1.B35130.

[8] Papamoschou, D., Xiong, J., and Liu, F., "Reduction of Radiation Efficiency in High-Speed Jets," *AIAA Paper 2014-2619*, 2014. https://doi.org/10.2514/6.2014-2619.

[9] Stuber, M., Lowe, K., and Wing, F., "Synthesis of Convection Velocity and Turbulence Measurements in Three-Stream Jets," *Experiments in Fluids*, Vol. 60, No. 83, 2019, pp. 998–1001. https://doi.org/10.1007/s00348-019-2730-5.

[10] Papamoschou, D., "On the Connection Between Near and Far Pressure Fields of a Turbulent Jet," *AIAA Paper 2018-1251*, 2018. https://doi.org/10.2514/6.2018-1251.

[11] Harper-Bourne, M., "Jet Noise Turbulence Measurements," *AIAA Paper 2003-3214*, 2003. https://doi.org/10.2514/6.2003-3214.

[12] Morris, P., and Zaman, K., "Velocity Measurements in Jets with Application to Jet Noise," *Journal of Sound and Vibration*, Vol. 329, 2010, pp. 394–414. https://doi.org/10.1016/j.jsv.2009.09.024.

[13] Proença, A., Lawrence, J., and Self, R., "Measurements of the Single-Point and Joint Turbulence Statistics of High Subsonic Jets Using Hot-Wire Anemometry," *Experiments in Fluids*, Vol. 60, No. 63, 2019. https://doi.org/10.1007/s00348-019-2716-3.

[14] Fleury, V., Bailly, C., Jondeau, E., Michard, M., and Juvé, D., "Space-Time Correlations in Two Subsonic Jets Using Dual Particle Image Velocimetry Measurements," *AIAA Journal*, Vol. 46, No. 10, 2008, pp. 2498–2509. https://doi.org/10.2514/1.35561.

[15] Pokora, C., and McGuirk, J., "Stereo-PIV Measurements of Spatio-Temporal Turbulence Correlations in an Axisymmetric Jet," *Journal of Fluid Mechanics*, Vol. 778, 2015, p. 216–252. https://doi.org/10.1017/jfm.2015.362.

[16] Adam, A., Papamoschou, D., Xiong, J., and Liu, F., "The Very Near Pressure Field of Three-Stream Jets," *AIAA Paper 2018-1739*, 2018. https://doi.org/10.2514/6.2018-1739.

[17] Adam, A., Papamoschou, D., Xiong, J., and Liu, F., "Vorticity Dynamics and Flow Statistics Near the Edge of HIgh Speed Multi-Stream Jets," *AIAA Paper 2019-1303*, 2019. https://doi.org/10.2514/6.2019-1303.

[18] Bogey, C., Marsden, O., and Bailly, C., "Large-Eddy Simulation of the Flow and Acoustic Fields of a Reynolds Number 10^5 Subsonic Jet With Tripped Exit Boundary Layers," *Physics of Fluids*, Vol. 23, No. 3, 2011, p. 035104. https://doi.org/10.1063/1.3555634.

[19] Bogey, C., Marsden, O., and Bailly, C., "Influence of Initial Turbulence Level on the Flow and Sound Fields of a Subsonic Jet at a Diameter-Based Reynolds Number of 10^5," *Journal of Fluid Mechanics*, Vol. 701, 2012, pp. 352–385. https://doi.org/10.1017/jfm.2012.162.

[20] Bogey, C., "Grid Sensitivity of Flow Field and Noise of High-Reynolds-number Jets Computed by Large-Eddy Simulation," *International Journal of Aeroacoustics*, Vol. 17, No. 4-5, 2018, pp. 399–424. https://doi.org/10.1177/1475472X18778287.

[21] Bogey, C., "Two-Dimensional Features of Correlations in the Flow and Near Pressure Fields of Mach Number 0.9 Jets," *AIAA Paper 2019-0806*, 2019. https://doi.org/10.2514/6.2019-0806.

[22] Bogey, C., "Acoustic tones in the near-nozzle region of jets: characteristics and variations between Mach numbers 0.5 and 2," *Journal of Fluid Mechanics*, Vol. 921, 2021, p. A3. https://doi.org/10.1017/jfm.2021.426.

[23] Zaman, K. B. M. Q., "Effect of Initial Condition on Subsonic Jet Noise," *AIAA Journal*, Vol. 23, No. 9, 1985, pp. 1370–1373. https://doi.org/10.2514/3.9094.

[24] Bogey, C., and Bailly, C., "Influence of Nozzle-Exit Boundary-Layer Conditions on the Flow and Acoustic Fields of Initially Laminar Jets," *Journal of Fluid Mechanics*, Vol. 663, 2010, p. 507–538. https://doi.org/10.1017/S0022112010003605.

[25] Bogey, C., Marsden, O., and Bailly, C., "Effects of Moderate Reynolds Numbers on Subsonic Round Jets With Highly Disturbed Nozzle-Exit Boundary Layers," *Physics of Fluids*, Vol. 24, No. 10, 2012, p. 105107. https://doi.org/10.1063/1.4757667.

[26] Bogey, C., and Marsden, O., "Identification of the Effects of the Nozzle-Exit Boundary-Layer Thickness and Its Corresponding Reynolds Number in Initially Highly Disturbed Subsonic Jets," *Physics of Fluids*, Vol. 25, No. 5, 2013, p. 055106. https://doi.org/10.1063/1.4807071.

[27] Bogey, C., and Sabatini, R., "Effects of Nozzle-Exit Boundary-Layer Profile on the Initial Shear-Layer Instability, Flow Field and Noise of Subsonic Jets," *Journal of Fluid Mechanics*, Vol. 876, 2019, p. 288–325. https://doi.org/10.1017/jfm.2019.546.

[28] Bogey, C., "Generation of Excess Noise by Jets with Highly Disturbed Laminar Boundary-Layer Profiles," *AIAA Journal*, Vol. 59, No. 2, 2021, pp. 569–579. https://doi.org/10.2514/1.J059610.

[29] Mohseni, K., and Colonius, T., "Numerical Treatment of Polar Coordinate Singularities," *Journal of Computational Physics*, Vol. 157, No. 2, 2000, pp. 787 – 795. https://doi.org/10.1006/jcph.1999.6382.

[30] Bogey, C., de Cacqueray, N., and Bailly, C., "Finite Differences for Coarse Azimuthal Discretization and for Reduction of Effective Resolution Near Origin of Cylindrical Flow Equations," *Journal of Computational Physics*, Vol. 230, No. 4, 2011, pp. 1134 – 1146. https://doi.org/10.1016/j.jcp.2010.10.031.

[31] Bogey, C., and Bailly, C., "A Family of Low Dispersive and Low Dissipative Explicit Schemes for Flow and Noise Computations," *Journal of Computational Physics*, Vol. 194, No. 1, 2004, pp. 194 – 214. https://doi.org/10.1016/j.jcp.2003.09.003.

[32] Bogey, C., de Cacqueray, N., and Bailly, C., "A Shock-Capturing Methodology Based on Adaptative Spatial Filtering for High-Order Non-Linear Computations," *Journal of Computational Physics*, Vol. 228, No. 5, 2009, pp. 1447 – 1465. https://doi.org/10.1016/j.jcp.2008.10.042.

[33] Tam, C. K., and Dong, Z., "Radiation and Outflow Boundary Conditions for Direct Computation of Acoustic and Flow Disturbances in a Nonuniform Mean Flow," *Journal of Computational Acoustics*, Vol. 04, No. 02, 1996, pp. 175–201. https://doi.org/10.1142/S0218396X96000040.

[34] Bogey, C., and Bailly, C., "Large Eddy Simulations of Transitional Round Jets: Influence of the Reynolds Number on Flow Development and Energy Dissipation," *Physics of Fluids*, Vol. 18, No. 6, 2006, p. 065101. https://doi.org/10.1063/1.2204060.

[35] Bogey, C., and Bailly, C., "Turbulence and Energy Budget in a Self-Preserving Round Jet: Direct Evaluation Using Large Eddy Simulation," *Journal of Fluid Mechanics*, Vol. 627, 2009, p. 129–160. https://doi.org/10.1017/S0022112009005801.

[36] Fauconnier, D., Bogey, C., and Dick, E., "On the Performance of Relaxation Filtering for Large-Eddy Simulation," *Journal of Turbulence*, Vol. 14, No. 1, 2013, pp. 22–49. https://doi.org/10.1080/14685248.2012.740567.

[37] Kremer, F., and Bogey, C., "Large-Eddy Simulation of Turbulent Channel Flow Using Relaxation Filtering: Resolution Requirement and Reynolds Number Effects," *Computers & Fluids*, Vol. 116, 2015, pp. 17 – 28. https://doi.org/10.1016/j.compfluid.2015.03.026.

[38] Dahl, M., "Turbulent Statistics from Time-Resolved PIV Measurements of a Jet Using Empirical Mode Decomposition," *AIAA Paper 2012-2297*, 2012. https://doi.org/10.2514/6.2012-2297.

[39] Kerhervé, F., Fitzpatrick, J., and Jordan, P., "The frequency dependence of jet turbulence for noise source modelling," *Journal of Sound and Vibration*, Vol. 296, No. 1, 2006, pp. 209 – 225. https://doi.org/10.1016/j.jsv.2006.02.012.

[40] Lau, J., Morris, P., and Fisher, M., "Measurements in Subsonic and Supersonic Free Jets Using a Laser Velocimeter," *Journal of Fluid Mechanics*, Vol. 93, No. 1, 1979, pp. 1–27.

[41] Papamoschou, D., Xiong, J., and Liu, F., "Towards a Low-Cost Wavepacket Model of the Jet Noise Source," *AIAA Paper 2015-1006*, 2015. https://doi.org/10.2514/6.2015-1006.

[42] Violato, D., and Scarano, F., "Three-Dimensional Vortex Analysis and Aeroacoustic Source Characterization of Jet Core Breakdown," *Physics of Fluids*, Vol. 25, No. 1, 2013, p. 015112. https://doi.org/10.1063/1.4773444.

[43] Picard, C., and Delville, J., "Pressure Velocity Coupling in a Subsonic Round Jet," *International Journal of Heat and Fluid Flow*, Vol. 21, No. 3, 2000, pp. 359 – 364. https://doi.org/10.1016/S0142-727X(00)00021-7.

[44] Coiffet, F., Jordan, P., Delville, J., Gervais, Y., and Ricaud, F., "Coherent Structures in Subsonic Jets: A Quasi-Irrotational Source Mechanism?" *International Journal of Aeroacoustics*, Vol. 5, No. 1, 2006, pp. 67–89. https://doi.org/10.1260/147547206775220407.

[45] Camussi, R., and Bogey, C., "Intermittent Statistics of the 0-Mode Pressure Fluctuations in the Near Field of Mach 0.9 Circular Jets at Low and High Reynolds Numbers," *Theoretical and Computational Fluid Dynamics*, Vol. 35, No. 2, 2021, pp. 229–247. https://doi.org/10.1007/s00162-020-00553-9.

[46] Arndt, R., Long, D., and Glauser, M., "The Proper Orthogonal Decomposition of Pressure Fluctutations Surrounding a Turbulent Jet," *Journal of Fluid Mechanics*, Vol. 340, 1997, pp. 1–33. https://doi.org/10.1017/S0022112097005089.

[47] Cavalieri, A. V. G., Jordan, P., Colonius, T., and Gervais, Y., "Axisymmetric Superdirectivity in Subsonic jets," *Journal of Fluid Mechanics*, Vol. 704, 2012, p. 388–420. https://doi.org/10.1017/jfm.2012.247.

[48] Bridges, J., "Rapid Prediction of Installed Jet Noise From RANS," *AIAA Paper 2019-2732*, 2019. https://doi.org/10.2514/6.2019-2732.

[49] Georgiadis, N., and DeBonis, J., "Navier-Stokes Analysis Methods for Turbulent Jet Flows with Application to Aircraft Exhaust Nozzles," *Progress in Aerospace Sciences*, Vol. 42, 2006, p. 378–418. https://doi.org/10.1016/j.paerosci.2006.12.001.

[50] Darisse, A., Lemay, J., and Benaïssa, A., "Budgets of Turbulent Kinetic Energy, Reynolds Stresses, Variance of Temperature Fluctuations and Turbulent Heat Fluxes in a Round Jet," *Journal of Fluid Mechanics*, Vol. 774, 2015, p. 95–142. https://doi.org/10.1017/jfm.2015.245.